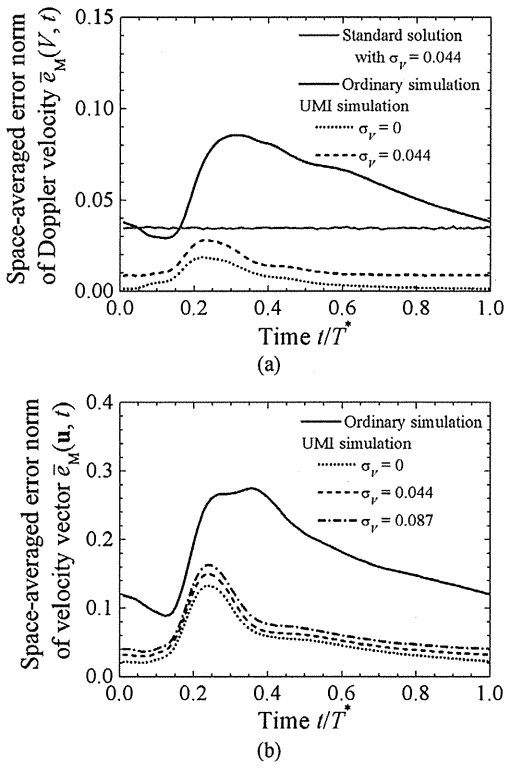

Fig. 6. Comparison of space-averaged error norms of (a) Doppler velocity and (b) of velocity vector among the standard solution affected by Gaussian noise, the ordinary simulation without feedback, and UMI simulations at each optimum feedback gain.

reduces error derived from inaccurate boundary conditions for the sake of feedback. More importantly, the value of $\bar{e}_{\mathrm{M}}(V, t)$ of the UMI simulation (a dashed line in Fig. 6(a)) was smaller than that of the standard solution with noise itself (a gray line in Fig. 6(a)). This indicates the possibility that the UMI simulation provides a result close to the true Doppler velocity more precisely than the ultrasonic measurement affected by noise. Variations of space-averaged error norm of the velocity vector, $\bar{e}_{\mathrm{M}}(\mathbf{u}, t)$, are shown in Fig. 6(b). At every time moment, the results of the UMI simulations are much smaller than that of the ordinary simulation, implying that the effect of noise included in the standard solution is minute.

The reason why the UMI simulation using the standard solution with Gaussian noise makes the computational result approach the true standard solution without deterioration of the computational accuracy is that the method calculates the velocity and pressure fields to satisfy the governing equations. The divergence of the feedback signals in the pressure equation of Eq. (2) does not become zero because of the noise included in the standard solution. However, components of the standard solution buried in the noise approach the above term zero and the result of the UMI simulation approaches the true standard solution. Therefore, even if noise included in the standard solution is applied for the feedback in the UMI simulation, it hardly influences the computational result.

As an example of visualization of the blood flow field, contours of Doppler velocity on multiple cross sections of the aneurysm and the parent artery at the timing of the maximum flow rate ($t/T^* = 0.13$ (0.13s)) are represented in Fig. 7. Because of the existence of a vortex in the aneurysm, velocity components of blood flow approaching and leaving an ultrasound probe exist, resulting in a mosaic pattern with warm and cold colors. Compared with the color Doppler image of the standard solution without measurement errors in Fig. 7(a), mottling can be observed in Fig. 7(b) under the influence of the noise ($\sigma_V = 0.087$). On the other hand, the color Doppler image of the UMI simulation in Fig. 7(c) has no mottling and resembles Fig. 7(a), though the standard solution with noise (see Fig. 7(b)) was used in the process of feedback.

B. *Effect of Aliasing*

This subsection discusses effect and treatment of aliasing in the UMI simulation. In Fig. 8(a), variations of time-space-averaged and space-averaged error norms of velocity vector, $\bar{e}_{MT^*}(\mathbf{u})$ and $\bar{e}_{\mathrm{M}}(\mathbf{u}, t)$, with feedback gain (left figure) and with time (right figure) are compared between the UMI simulations using the standard solution with/without aliasing ($|V_{\mathrm{thre}}| = 0.22$, 0.44, 0.87 and 1.09) and the ordinary simulation without feedback ($K_{\mathrm{v}}^* = 0$). In the case of $|V_{\mathrm{thre}}| = 0.22$, the error norm, $\bar{e}_{MT^*}(\mathbf{u})$, of the UMI simulation monotonically increases as the feedback gain increases (see the left figure in Fig. 8(a)). In cases that the measurable Doppler velocity range is relatively large ($|V_{\mathrm{thre}}| > 0.44$), the error norm of the UMI simulation in the proper condition is smaller than that of the ordinary simulation, even if aliasing occurs in the standard solution. Note that $\bar{e}_{MT^*}(\mathbf{u})$ evaluates the error of velocity vector by averaging in one cardiac cycle. Evaluation of the error at each time moment with the error norm of $\bar{e}_{\mathrm{M}}(\mathbf{u}, t)$ shows that there are timings when the computational accuracy of the UMI simulation becomes worse than that of the ordinary simulation by using an aliased standard solution for feedback (see the right figure in Fig. 8(a)). As seen in the result of the case of $|V_{\mathrm{thre}}| = 1.09$, even though the duration of aliasing is short with a small percentage of aliased points in the feedback points (see Fig. 4(a)), instantaneous deterioration of the computational accuracy occurs in systole and the effect remains after that. Thus, the UMI simulation works to reproduce the aliasing included in the standard solution, and the computational accuracy becomes worse.

When aliased data is applied for feedback, the magnitude of feedback signal at the feedback point becomes abnormally large since the Doppler velocity drastically changes compared with those around the point. The authors have previously proposed a treatment method for aliasing in a study concerning two-dimensional UMI simulation of the blood flow field [20]. In this study, the treatment method was also examined in the 3-D UMI simulation, i.e., by detecting the cases of $|\mathbf{\Phi}_1(\mathbf{u}_{\mathrm{c}} - \mathbf{u}_{\mathrm{s}})| > |V_{\mathrm{thre}}|$, application of a feedback signal was cancelled at the feedback point. Error norms, $\bar{e}_{MT^*}(\mathbf{u})$ and $\bar{e}_{\mathrm{M}}(\mathbf{u}, t)$, of the UMI simulation with the above treatment for aliasing are shown in Fig. 8(b). Compared with Fig. 8(a), the error norms decrease in all the cases, implying that the aliasing is successfully detected and canceled. The values of UMI simulations are almost the

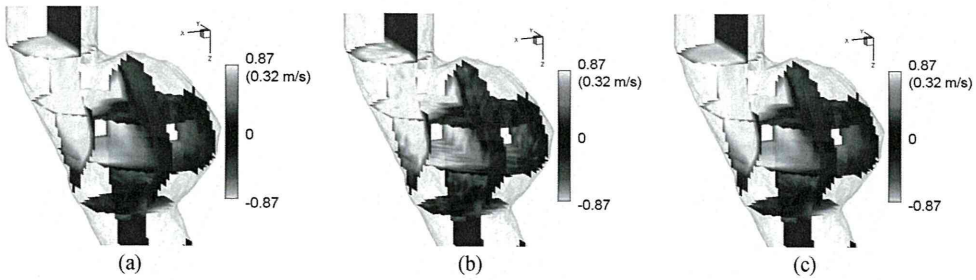

Fig. 7. Contour maps of Doppler velocity on four horizontal and three vertical planes at peak flow ($t/T^* = 0.13$): the standard solutions (a) without measurement errors and (b) with Gaussian noise of $\sigma_V = 0.087$ (3.2 cm/s in dimensional value), and the UMI simulation using the data "(b)" for feedback at $K_v^* = 11$.

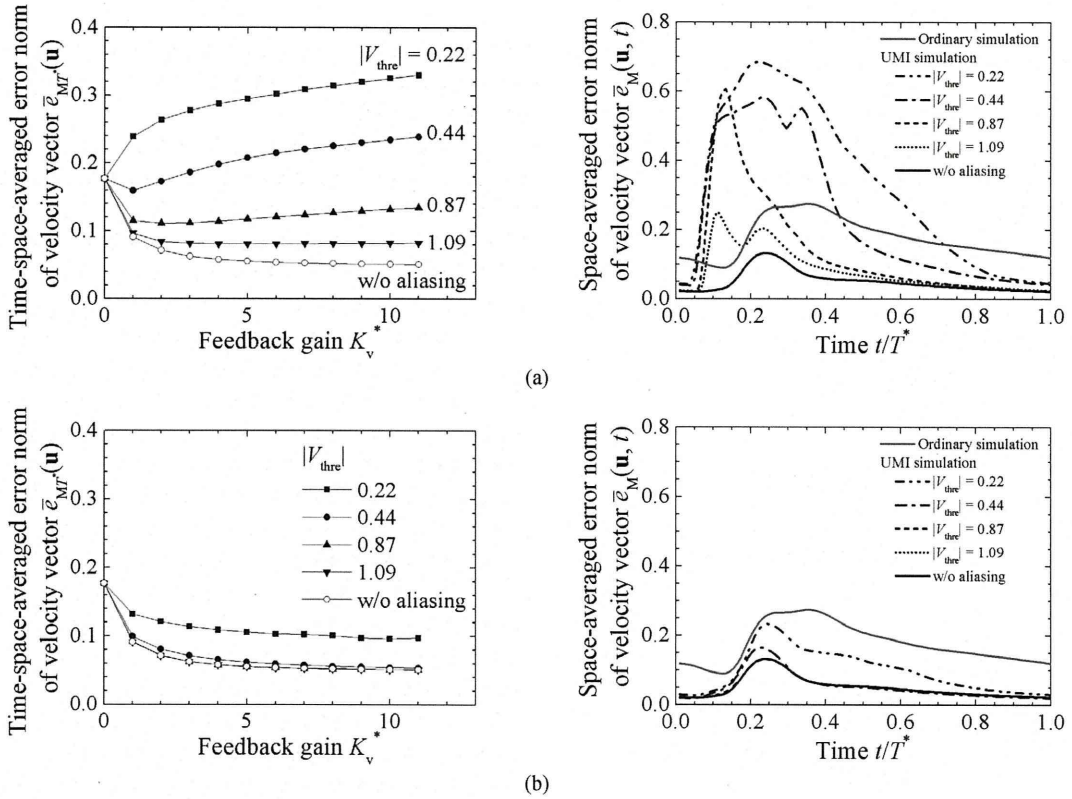

Fig. 8. Time-space-averaged (left column) and space-averaged error norms (right column) of the velocity vector of UMI simulations using aliased standard solution (a) without and (b) with a detection method for aliasing at $K_v^* = 11$.

same as that of the UMI simulation using the nonaliased standard solution except for the case of $|V_{\mathrm{thre}}| = 0.22$.

The contours of Doppler velocity on multiple cross sections of the aneurysm and the parent artery of the standard solution with aliasing ($|V_{\mathrm{thre}}| = 0.87$) at the timing of the maximum flow rate are represented in Fig. 9(a). Different from Fig. 7(a), displays with a reversal of colors are visible at locations where the Doppler velocity exceeds the threshold $|V_{\mathrm{thre}}|$: a region with cold color in the parent artery mainly on the leftmost vertical cross section (see a white arrow in Fig. 9(a)) and in a region with warm color at the neck of the aneurysm on the lowest horizontal cross section (see a black arrow). Using the standard solution with aliasing in the UMI simulation, feedback signals work in incorrect directions at the aliased points, resulting in a dark display, as shown in Fig. 9(b). In contrast, as shown in Fig. 9(c), a color Doppler image of the UMI simulation with the treatment for aliasing well reproduces the standard solution without measurement error of Fig. 7(a).

C. *Effect of Wall Filter*

In this subsection, the effect of wall filter, which forces small Doppler velocity to zero in the ultrasonic measurement, is evaluated.

Fig. 10(a) represents the relationship between the time-space-averaged error norm of velocity vector, $\bar{e}_{MT^*}(\mathbf{u})$, and the feedback gain, K_v^*, of the UMI simulations using the standard solutions in which small Doppler velocities are zeroed with wall filters ($|V_{\mathrm{WF}}| = 0.022$ or 0.087). Similar to the effect by Gaussian noise (see Fig. 5), the value of $\bar{e}_{MT^*}(\mathbf{u})$ increases with K_v^* in UMI simulation with the feedback of the standard solution

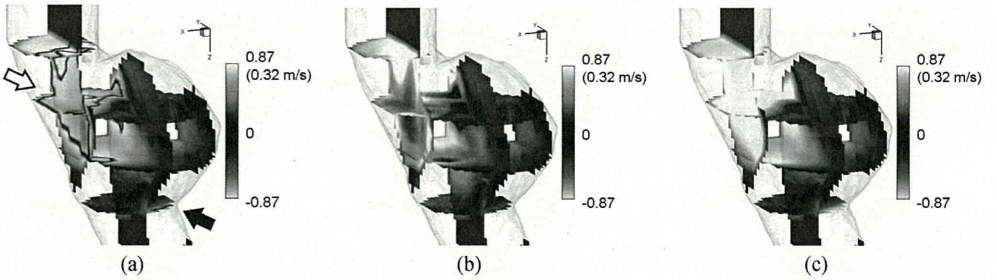

Fig. 9. Contour maps of Doppler velocity on four horizontal and three vertical planes at peak flow ($t/T^* = 0.13$): (a) the standard solution with aliasing with $|V_{\rm thre}| = 0.87$ (32 cm/s in dimensional value) and UMI simulations using the data "(a)" for feedback (b) without and (c) with detection method for aliasing at $K_{\rm v}^* = 11$. Black and white arrows indicate aliased regions.

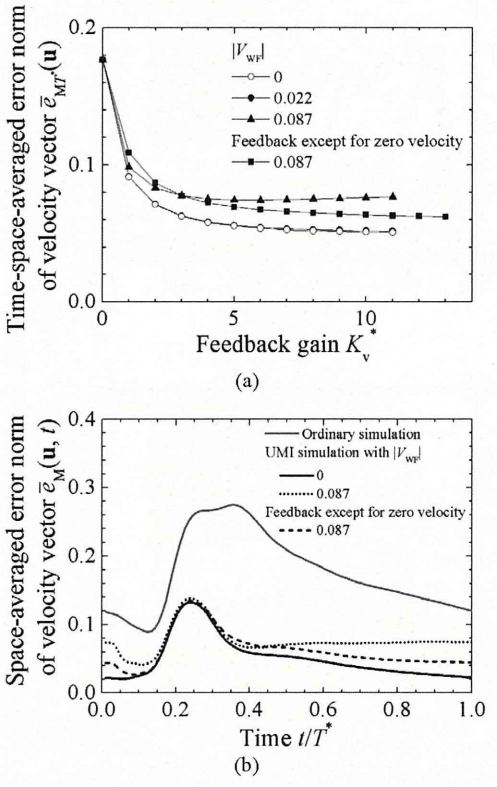

Fig. 10. (a) Variation of time-space-averaged error norm of velocity vector with feedback gain and (b) space-averaged error norm of velocity vector of UMI simulations with different degrees of wall filter, $|V_{\rm WF}|$, for feedback.

being processed by a wall filter with a relatively large value of $|V_{\rm WF}| = 0.087$. In this study, the effect of a wall filter on the UMI simulation was negligible in $|V_{\rm WF}| \leq 0.044$. This means that Doppler velocities reset to zero are originally slow, so that they do not much affect the whole flow field through the feedback process.

The computational accuracy of the UMI simulation ($K_{\rm v}^* = 11$) using the standard solution with the wall filter with $|V_{\rm WF}| = 0.087$ is evaluated at each time moment by the space-averaged error norm of the velocity vector, $\bar{e}_{\rm M}(\mathbf{u}, t)$ (see a dotted line in Fig. 10(b)). Enlargement of the error norm from the UMI simulation using the standard solution without the wall filter (black line) is observed, especially in diastole. This is because the information of Doppler velocity of the standard solution at many feedback points tends to be lost in diastole, being reset to zero (see Fig. 4(b)).

To prevent the feedback of filtered zero Doppler velocity in the UMI simulation, application of feedback signals was skipped at feedback points whose Doppler velocities of standard solution processed by a wall filter were zero. In Fig. 10, the error norms of the UMI simulation with treatment are also shown. With the treatment, the maximum value of feedback gain, with which numerical solution can be obtained without divergence, increases up to $K_{\rm v}^* = 13$ in the UMI simulation using the standard solution with the wall filter with $|V_{\rm WF}| = 0.087$ (see Fig. 10(a)). The value of $\bar{e}_{MT^*}(\mathbf{u})$ is repressed so as not to increase with the feedback gain by the treatment for the wall filter, though it is larger than that without the treatment in the range of small feedback gain. In the space-averaged error norm of the velocity vector in Fig. 10(b), a decrease of the error by the treatment is visible in diastole, showing a result equivalent to the UMI simulation using the standard solution without a wall filter ($|V_{\rm WF}| = 0$).

Contours of Doppler velocity of the standard solution on multiple cross sections in the aneurysm and the parent artery at $t/T^* = 0.61$ (0.60 s, dimensionally) in diastole are shown in Fig. 11(a). Applying the wall filter with $|V_{\rm WF}| = 0.087$ to the standard solution, the velocity adjacent to the blood vessel wall becomes zero, resulting in enlargement of the black region, as shown in Fig. 11(b). The UMI simulation (see Fig. 11(c)) using the data of Fig. 11(b), but not applying the feedback signals at feedback points whose Doppler velocities are zero, is similar to the standard solution without measurement errors of Fig. 11(a) for the sake of feedback. In contrast, the ordinary simulation without the feedback provides different patterns of contours as shown in Fig. 11(d).

Actually, more complicated MTI filters developed by various manufacturers are installed in ultrasonic measurement equipment to visualize only blood flow in color Doppler imaging. However, the basic concept of such filters is to regard regions with small velocity as tissue, ignoring the slow velocities. Therefore, though the above investigation with regard to the wall filter, by which all slow velocities less than a threshold value were changed to zero, may not be complete, it gives us fundamental insights for repressing the effect of MTI filters on the UMI simulation.

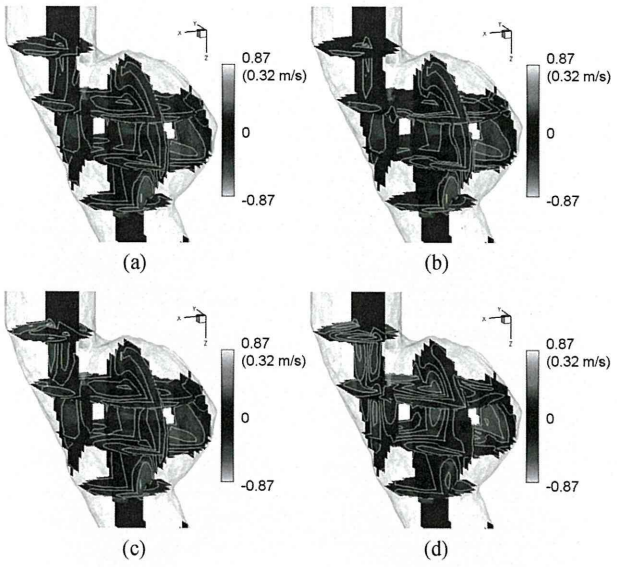

Fig. 11. Contour maps of Doppler velocity on four horizontal and three vertical planes in diastole ($t/T^* = 0.61$): standard solution (a) without and (b) with wall filter with $|V_{\mathrm{WF}}| = 0.087$ (3.2 cm/s in dimensional value), (c) UMI simulation using the data "(b)" for feedback except for zero velocity at $K_{\mathrm{v}}^* = 11$, and (d) ordinary simulation ($K_{\mathrm{v}}^* = 0$).

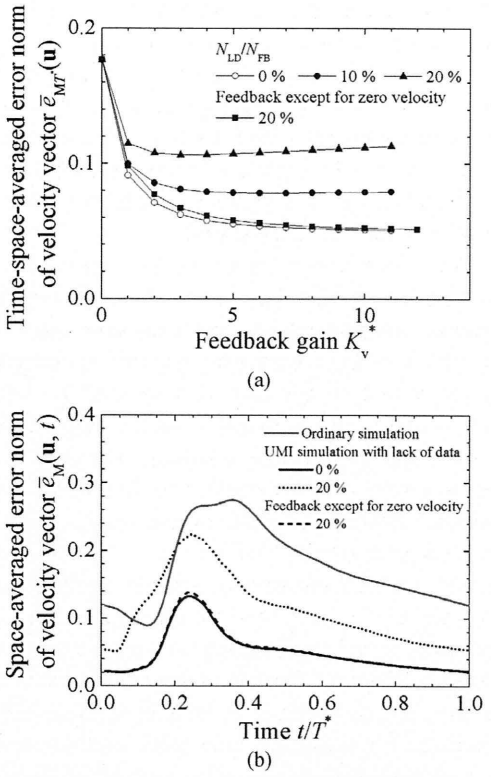

Fig. 12. (a) Variation of time-space-averaged error norm of velocity vector with feedback gain and (b) space-averaged error norm of velocity vector of UMI simulations with different degrees of lack of data for feedback.

D. *Effect of Lack of Data*

The time-space-averaged and space-averaged error norms of the velocity vector of the UMI simulation using the standard solution, whose Doppler velocities are randomly zeroed, are shown in Fig. 12. The error norms become large as the degree of the lack of data increases (see Fig. 12(a)). Especially in the cases with much lack of data ($N_{\mathrm{LD}}/N_{\mathrm{FB}} \geq 10\%$), error sharply decreases and then gradually increases with the feedback gain. Additionally, there are timings when the computational accuracy of the UMI simulation becomes worse than the ordinary simulation (see Fig. 12(b)).

Lack of data and wall filter are similar in terms of incorrect output of measured Doppler velocities as zero. Average percentages of feedback points whose Doppler velocities were processed by wall filters with $|V_{\mathrm{WF}}| = 0.011$, 0.022, 0.044, and 0.087 in one cardiac cycle were $N_{\mathrm{WF}}/N_{\mathrm{FB}} = 6.9\%$, 13.5%, 25.5%, and 45.2%, respectively (see Fig. 4). Comparison of the space-averaged error norms of Doppler velocity between UMI simulations using the standard solution with those having almost the same percentages of $N_{\mathrm{WF}}/N_{\mathrm{FB}}$ by a wall filter and $N_{\mathrm{LD}}/N_{\mathrm{FB}}$ by a lack of data (see Figs. 10(b) and 12(b)), showed that error derived from the lack of data was more significant in the whole period. Accordingly, lack of measurement data has a greater influence on the UMI simulation than the wall filter since the fast Doppler velocity is reset as zero.

The same investigation as that for treatment of the wall filter was carried out for the lack of data; feedback was not applied at the feedback points whose Doppler velocities were zero. In Fig. 12, time-space-averaged and space-averaged error norms of the velocity vector of the UMI simulation with treatment for the lack of data ($N_{\mathrm{LD}}/N_{\mathrm{FB}} = 20\%$) are also shown. Only in the case of a lack of 20% of the data, a numerical solution without

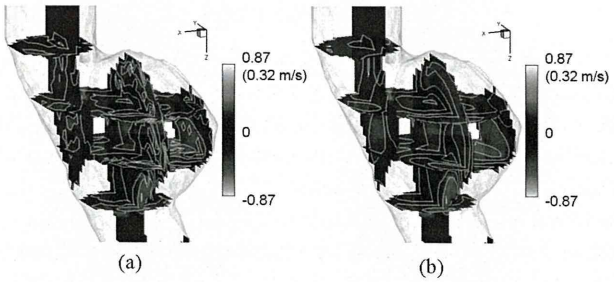

Fig. 13. Contour maps of Doppler velocity on four horizontal and three vertical planes in diastole ($t/T^* = 0.61$): (a) standard solution with lack of 20% of data, and (b) UMI simulation using the data "(a)" for feedback except for zero velocity at $K_{\mathrm{v}}^* = 11$.

divergence is obtained even with the feedback gain of $K_{\mathrm{v}}^* = 12$ in the UMI simulation. Owing to the treatment for a lack of data, the UMI simulation becomes able to provide almost the same result as that using the standard solution without measurement errors.

The result of Doppler velocities of the standard solution with a lack of 20% of the data at the same timing ($t/T^* = 0.61$) in Fig. 11 is visualized in Fig. 13(a). Since the Doppler velocities are randomly zeroed, the contour has many black dots, being different from Fig. 11(a). On the other hand, in Fig. 13(b), the UMI simulation using the standard solution of Fig. 13(a) but not applying the feedback at feedback points whose Doppler velocities are zero well reproduces the standard solution without lack of data of Fig. 11(a).

In ultrasonic measurement, there are two cases by which Doppler velocity becomes zero: blood flow velocity is actually zero, and the velocity is affected by measurement errors. Although it is difficult to distinguish them, it is possible to make the computational result approach the true blood flow field and to improve the computational accuracy by not applying feedback signals in cases in which the measured Doppler velocities are zero in the UMI simulation.

In the above discussion, effects of four measurement errors were investigated independently. But in a real situation, these errors appear simultaneously, and Gaussian noise may lead Doppler velocity to aliasing or zero velocity by increasing or decreasing the velocity magnitude. A combination of the present treatments is probably a solution in such a case, but it remains as a future work. In addition, scanning sequence and time in ultrasonic measurement were neglected. In order to more realistically mimic ultrasonic Doppler measurement, a sophisticated way has been proposed by Swillens *et al.* [21], [22], including the dynamics of scan sequencing and the statistics of velocity estimation process in ultrasound color Doppler imaging. In contrast, this study aimed at clarifying how each error in ultrasonic measurement influenced the blood flow field, especially in the 3-D velocity vectors, obtained by UMI simulation in detail. The results indicate the possibility that UMI simulation with treatments for aliasing and zero Doppler velocity at an appropriate feedback gain ($K_v^* < 12$) reproduces the blood flow field.

IV. Conclusion

Among measurement errors included in ultrasound Doppler measurement, effects of four major measurement errors, namely, those due to Gaussian noise, aliasing, wall filter, and lack of data, on UMI simulation were examined by a numerical experiment dealing with the same objective of blood flow field in the descending aorta with an aneurysm as that in our previous study. While solving the governing equations in a UMI simulation, Gaussian noise did not prevent the UMI simulation from effectively reproducing the blood flow field. In contrast, aliasing caused significant errors in the UMI simulation. Effects of wall filter and lack of data appeared in diastole and in the whole period, respectively. By detecting significantly large feedback signals as a sign of aliasing and by not adding feedback signals where measured Doppler velocities were aliasing or zero, the computational accuracy substantially improved, alleviating the effects of measurement errors. Based on these considerations, UMI simulation can be performed with suppression of four major measurement errors, and accurately provides detailed information on hemodynamics.

Acknowledgment

All computations were performed using the supercomputer system (SGI Altix 3700 B×2, SGI Japan, Tokyo, Japan) at the Advanced Fluid Information (AFI) Research Center, Institute of Fluid Science, Tohoku University.

References

[1] N. Depaola, M. A. Gimbrone, P. F. Davies, and C. F. Dewey, "Vascular endothelium responds to fluid shear-stress gradients," *Arterioscler. Thrombosis*, vol. 12, pp. 1254–1257, Nov. 1992.

[2] M. J. Levesque and R. M. Nerem, "The elongation and orientation of cultured endothelial-cells in response to shear-stress," *J. Biomech. Eng. Trans. ASME*, vol. 107, pp. 341–347, 1985.

[3] E. Sho, M. Sho, K. Hoshina, H. Kimura, T. K. Nakahashi, and R. L. Dalman, "Hemodynamic forces regulate mural macrophage infiltration in experimental aortic aneurysms," *Exp. Mol. Pathol.*, vol. 76, pp. 108–116, Apr. 2004.

[4] J. Suo, D. E. Ferrara, D. Sorescu, R. E. Guldberg, W. R. Taylor, and D. P. Giddens, "Hemodynamic shear stresses in mouse aortas—Implications for atherogenesis," *Arterioscler. Thrombosis Vascular Biol.*, vol. 27, pp. 346–351, Feb. 2007.

[5] D. A. Steinman, "Image-based computational fluid dynamics modeling in realistic arterial geometries," *Ann. Biomed. Eng.*, vol. 30, pp. 483–497, Apr. 2002.

[6] T. Hassan, E. V. Timofeev, T. Saito, H. Shimizu, M. Ezura, T. Tominaga, A. Takahashi, and K. Takayama, "Computational replicas: Anatomic reconstructions of cerebral vessels as volume numerical grids at three-dimensional angiography," *Amer. J. Neuroradiol.*, vol. 25, pp. 1356–1365, Sep. 2004.

[7] M. Shojima, M. Oshima, K. Takagi, R. Torii, M. Hayakawa, K. Katada, A. Morita, and T. Kirino, "Magnitude and role of wall shear stress on cerebral aneurysm—Computational fluid dynamic study of 20 middle cerebral artery aneurysms," *Stroke*, vol. 35, pp. 2500–2505, Nov. 2004.

[8] C. K. Zarins, D. P. Giddens, B. K. Bharadvaj, V. S. Sottiurai, R. F. Mabon, and S. Glagov, "Carotid Bifurcation atherosclerosis quantitative correlation of plaque localization with flow velocity profiles and wall shear-stress," *Circ. Res.*, vol. 53, pp. 502–514, 1983.

[9] E. S. Di Martino, G. Guadagni, A. Fumero, G. Ballerini, R. Spirito, P. Biglioli, and A. Redaelli, "Fluid–structure interaction within realistic three-dimensional models of the aneurysmatic aorta as a guidance to assess the risk of rupture of the aneurysm," *Med. Eng. Phys.*, vol. 23, pp. 647–655, Nov. 2001.

[10] K. R. Moyle, L. Antiga, and D. A. Steinman, "Inlet conditions for image-based CFD models of the carotid bifurcation: Is it reasonable to assume fully developed flow?" *J. Biomech. Eng. Trans. ASME*, vol. 128, pp. 371–379, Jun. 2006.

[11] T. Hayase and S. Hayashi, "State estimator of flow as an integrated computational method with the feedback of online experimental measurement," *J. Fluids Eng. Trans. ASME*, vol. 119, pp. 814–822, Dec. 1997.

[12] K. Nisugi, T. Hayase, and A. Shirai, "Fundamental study of hybrid wind tunnel integrating numerical simulation and experiment in analysis of flow field," *JSME Int. J. Ser. B Fluids Therm. Eng.*, vol. 47, pp. 593–604, Aug. 2004.

[13] T. Yamagata, T. Hayase, and H. Higuchi, "Effect of feedback data rate in PIV measurement-integrated simulation," *J. Fluid Sci. Technol.*, vol. 3, pp. 477–487, 2008.

[14] M. Nakao, K. Kawashima, and T. Kagawa, "Application of MI simulation using a turbulent model for unsteady orifice flow," *J. Fluids Eng. Trans. ASME*, vol. 131, pp. 111401-1–6, Nov. 2009.

[15] K. Funamoto, T. Hayase, Y. Saijo, and T. Yambe, "Numerical experiment of transient and steady characteristics of ultrasonic-measurement-integrated simulation in three-dimensional blood flow analysis," *Ann. Biomed. Eng.*, vol. 37, pp. 34–49, Jan. 2009.

[16] K. Funamoto, T. Hayase, Y. Saijo, and T. Yambe, "Numerical experiment for ultrasonic-measurement-integrated simulation of three-dimensional unsteady blood flow," *Ann. Biomed. Eng.*, vol. 36, pp. 1383–1397, Aug. 2008.

[17] K. Funamoto, Y. Suzuki, T. Hayase, T. Kosugi, and H. Isoda, "Numerical validation of MR-measurement-integrated simulation of blood flow in a cerebral aneurysm," *Ann. Biomed. Eng.*, vol. 37, pp. 1105–1116, Jun. 2009.

[18] K. Funamoto, T. Hayase, A. Shirai, Y. Saijo, and T. Yambe, "Fundamental study of ultrasonic-measurement-integrated simulation of real blood flow in the aorta," *Ann. Biomed. Eng.*, vol. 33, pp. 415–428, Apr. 2005.

[19] M. S. Olufsen, C. S. Peskin, W. Y. Kim, E. M. Pedersen, A. Nadim, and J. Larsen, "Numerical simulation and experimental validation of blood flow in arteries with structured-tree outflow conditions," *Ann. Biomed. Eng.*, vol. 28, pp. 1281–1299, Nov./Dec. 2000.

[20] K. Funamoto, T. Hayase, Y. Saijo, and T. Yambe, "Detection and correction of aliasing in ultrasonic measurement of blood flows with ultrasonic-measurement-integrated simulation," *Technol. Health Care*, vol. 13, pp. 331–344, Jul. 2005.
[21] A. Swillens, T. De Schryver, L. Lovstakken, H. Torp, and P. Segers, "Assessment of numerical simulation strategies for ultrasonic color blood flow imaging, based on a computer and experimental model of the carotid artery," *Ann. Biomed. Eng.*, vol. 37, pp. 2188–2199, Nov 2009.
[22] A. Swillens, L. Lovstakken, J. Kips, H. Torp, and P. Segers, "Ultrasound simulation of complex flow velocity fields based on computational fluid dynamics," *IEEE Trans. Ultrason. Ferroelectr. Freq. Control*, vol. 56, pp. 546–556, Mar. 2009.

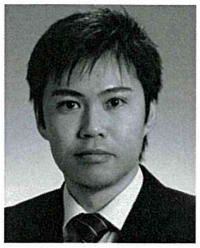

Kenichi Funamoto was born in Yamaguchi Prefecture, Japan, in 1979. He received the Ph.D. degree in engineering from Tohoku University, Sendai, Japan, in 2007.

Since 2008, he has been an Assistant Professor in the Institute of Fluid Science, Tohoku University. His current research interests include measurement-integrated simulation and blood flow analysis.

Toshiyuki Hayase was born in Nagoya, Japan, in 1956. He received the Ph.D. degree in engineering in 1987 from Nagoya University, Nagoya, Japan.

From 1980 to 1990, he was a Research Associate at Nagoya University. He became an Associate Professor of the Institute of Fluid Science, Tohoku University, Sendai, Japan, in 1990, and has been a Professor since 2000. His current research interests include the measurement-integrated simulation of complex flow problems.

Yoshifumi Saijo received the M.D. and Ph.D. degrees from Tohoku University, Sendai, Japan, in 1988 and 1993, respectively.

He is currently a Professor at the Graduate School of Biomedical Engineering, Tohoku University. His current research interests include high-resolution biomedical imaging with high-frequency ultrasound, blood flow analysis in the cardiovascular system, and parametric imaging with intravascular ultrasound or transesophageal echocardiography.

Tomoyuki Yambe received the Ph.D. degree in medicine from Tohoku University, Sendai, Japan, in 1989.

Since 2004, he has been a Professor in the Institute of Development, Aging and Cancer, Tohoku University. His current research interests include cardiology, artificial organs such as an artificial heart including totally implantable ventricular assist system, clinical application of ventricular assist devices, and an autonomic nervous system.

33rd Annual International Conference of the IEEE EMBS
Boston, Massachusetts USA, August 30 - September 3, 2011

Palpation Nonlinear Reaction Force Analysis for Characterization of Breast Tissues

Yo Kobayashi, *Member, IEEE,* Mariko Tsukune, Takeharu Hoshi, Tomoyuki Miyashita, Yasuyuki Shiraishi, Tomoyuki Yambe and Masakatsu G. Fujie, *Member, IEEE*

***Abstract*— This paper addresses a diagnostic palpation system based on the measurement of nonlinear elasticity. An indentation probe is used to press against breast tissue. Then, the measured reaction force is used to estimate the parameters of nonlinear elasticity, which enables the identification of tissue type, such as fat, muscle, mammary gland or tumor. Here, we present the basic concept of our study and preliminary experimental and simulation results from pilot studies. More specifically, we measured the nonlinear response of reaction force using the breast of a goat. In addition, we also simulated the reaction force using nonlinear biomechanical simulation with several tissue types. Large differences in reaction force occur only in the nonlinear range in both experimental and simulation situations. Our results confirmed the feasibility of our concept.**

I. Introduction

BREST cancer accounts for more than 1 million of the estimated 10 million malignancies diagnosed worldwide each year. In recent years, early detection of breast cancer has been possible because of advances in imaging technology. However, it is difficult to locate the exact position of a tumor and to make a definite diagnosis by palpation or imaging. In addition, invasive examinations such as biopsy are needed to diagnose whether a breast tumor is benign or malignant. Non-invasive and accurate diagnostic techniques are, therefore, desired to achieve accurate diagnosis and to alleviate the patient's mental burden.

The stiffness of malignant tumors has traditionally been qualitatively measured based on palpation by doctors. Many studies have reported systems for tissue characterization and for locating exact tumor position based on palpation. In particular, elastography imaging technologies have been explored. Elastography requires the induction of motion within the target tissue by an external force and conventional medical imaging modalities are used to measure tissue deformation, from which mechanical properties can be reconstructed.

There are limitations in the present elastography protocols. Elastography imaging typically provides contrast in linear stiffness under the assumption of very small deformations. It is actually very difficult to measure nonlinear properties using large deformations. On the other hand, tissues generally exhibit homogeneous, nonlinear, anisotropic elastic and viscous behaviors [1]. Krouskop et al. [2], Wellman et al. [3] and Samani et al. [4] measured the stiffness properties of breast tissues. These papers reported that breast tissue exhibits strong nonlinear properties. More specifically, tissues under low stress exhibit linear properties, but stiffness increased in tissues under high stress. The authors have also reported the measurement of nonlinear elastic properties of breast soft tissues, such as fatty tissue, muscles and mammary glands [5]. They reported that there are large differences in the magnitude of nonlinear elasticity among breast tissues, while differences in elastic properties in the linear range are small.

The goal of this study is to develop a diagnostic palpation system to identify the location of each tissue based on the measurement of nonlinear elasticity. Figure 1 shows our system concept. The indentation probe presses against breast tissue to the extent that the strains of breast tissue become large and such that nonlinear properties are exhibited. Then, the measured reaction force is used to estimate the parameters of nonlinear elasticity. The type of tissue, such as fat, muscle, mammary grand or tumor is identified by the estimated parameters of nonlinear elasticity. In addition, we consider that nonlinear elasticity measurement can be an effective method for the identification of tumor type because Krouskop et al. [2] have shown that nonlinear elasticity of malignant tumor is larger than that of benign tumor.

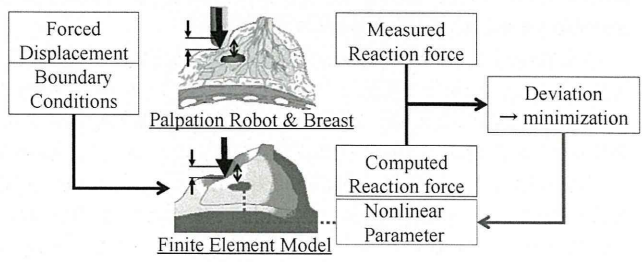

Fig.1. The conceptual scheme of our palpation method.

Manuscript received April 15th, 2011. This work was supported, in part, by the Global COE Program "Global Robot Academia" from MEXT (Ministry of Education, Culture, Sports, Science and Technology of Japan), a High-Tech Research Center Project from MEXT, a Grant-in-Aid for Scientific Research from MEXT (no. 22360108 and 22103512), a Waseda University Grant for Special Research Projects (no. 2010B-177) and Cooperative Research Project of the Institute of Development, Aging and Cancer, Tohoku University.

Y. Kobayashi is with the Faculty of Science and Engineering, Waseda University, Japan. (59-309, 3-4-1 Ohkubo Shinjuku-ku, Tokyo, Japan, phone: +81-3-5286-3412; fax: +81-3-5291-8269; e-mail: you-k@fuji.waseda.jp).

M. Tsukune is with the Graduate School of Science and Engineering, Waseda University, Japan.

T. Hoshi, T. Miyashita and M. G. Fujie are with the Faculty of Science and Engineering, Waseda University, Japan.

Y. Shiraishi and T. Yambe are with the Department of Medical Engineering and Cardiology, Institute of Development, Aging and Cancer, Tohoku University

978-1-4244-4122-8/11/$26.00 ©2011 IEEE

It should be noted that there are some studies in the field of elastography addressing nonlinear elasticity. For example, Hall et al. present a system for nonlinearity imaging by 1% incremental strain [6]. Nitta et al. have described nonlinear elasticity parameter estimations for kidney phantom [7]. Wang et al. present an elastography method for reconstruction of nonlinear breast tissue properties and for simulation investigation [8]. These papers propose methods to identify nonlinear parameters but experimental evaluation with actual animal tissues were not conducted [7] [8]. Hall et al. [6] reported experiments and evaluation with actual tissue, although the experiment was conducted with only small displacements. In short, tissue characterization using analysis of nonlinear reaction force with large deformation has not been conducted.

The objective of the present paper is to investigate the basic concept of our study using preliminary experimental and simulation studies. More specifically, we used goat breast to measure the reaction force in response to large deformation. In addition, we also simulated the reaction force using nonlinear biomechanical simulation in several tissue types. The feasibility of our concept, tissue identification based on nonlinear properties of tissues, is discussed.

II. METHOD

A. Experiment

In this section, we describe the conditions under which the in vivo experiment was conducted. The method was performed using a test apparatus implanted in the breast of a goat. We intended to measure the reaction force from two indentation points in which the ratio of tissues (fats and mammary gland) are different under each point. The experimental details are described below (Fig. 2).

1) Ethical issues: All animals received humane care in accordance with "The Guidelines for the Care and Use of Laboratory Animals" published by the National Institute of Health (NIH publication 85-23, revised 1985), "The Guidelines for Proper Conduct of Animal Experiments" formulated by the Science Council of Japan (2006), and the guidelines determined by the Institutional Animal Care and Use Committee of Tohoku University.

2) Experimental setup: A goat breast was used for in vivo experiments. The goat was placed supine as shown in Fig. 2. In humans, the sternum is located under the breast, which acts as a stiff boundary (refer to Fig. 3). Unlike humans, goats have no sternum under their breast. As a boundary condition, considering the effect of the sternum in humans, we set the dorsal area of the goat breast as the fixed boundary by inserting a metal plate as shown in Fig. 3.

3) Experimental apparatus: The experimental manipulator has one degree of freedom of linear movement by an actuator. A force sensor (NANO 1.2/1, BL AUTOTEC) and a 7 mm diameter indentation probe were attached to the manipulator as shown in Fig. 2. We calculated the moving distance of the probe from the value of the encoder attached to the motor. The reactive forces exerted on the probe were sampled by the force sensor.

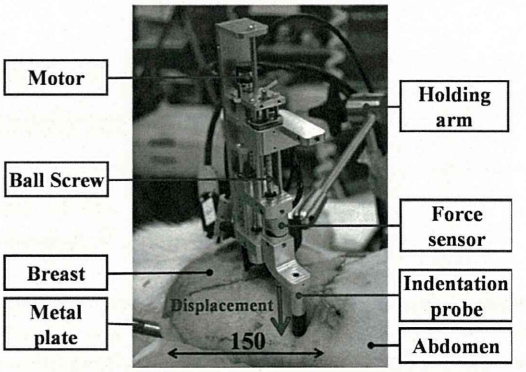

Fig.2. The arrangement of the goat breast and apparatus.

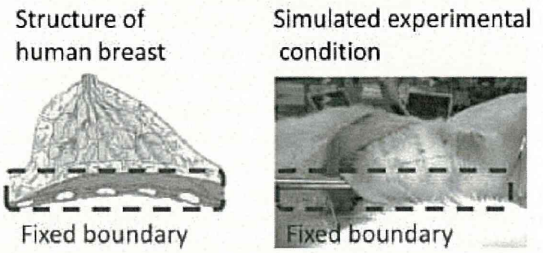

Fig.3. The boundary conditions of the breast in vivo.

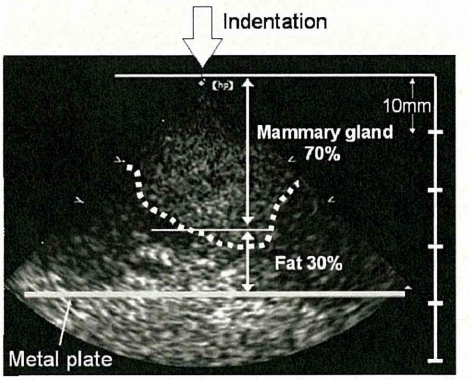

(a) Point A

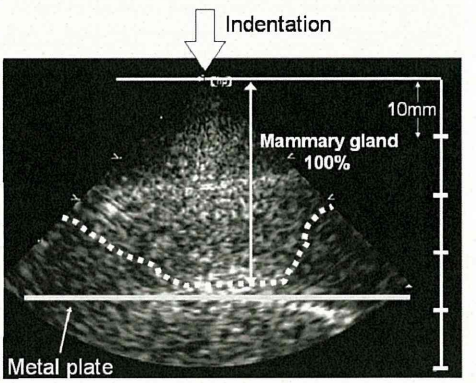

(b) Point B

Fig.4. Ultrasound images of hog breast at each point

4) Imaging modality: Ultrasound equipment (SONOS 5500, Hewlett Packard) was used for imaging because of its compatibility with the robot and for its ability to show real-time visualization.

5) Experimental conditions and procedures: First, we searched for an indentation point using an ultrasound probe. We judged the ratio of fats to mammary gland under the search point from the contrast of ultrasound images. We determined two points in which the ratio of fat and mammary grand are different: under point A, the tissue ratio was 70% mammary gland to 30% fat and at point B the tissue ratio was 100% mammary gland to 0% fat. The ultrasound images at each point are shown in Fig.4. For each point we positioned the experimental apparatus and fixed it in place using a laparoscope positioning device that can be changed between a free state and a locked state. The indentation was then carried out at constant velocity 3.0 mm/s and the force and displacement of the probe were recorded. Three indentations were performed at each point. We performed the experiment at point A and B.

B. Simulation

We have developed and reported mechanical liver and breast models in previous papers, in which we also gave specific descriptions of the material properties of the liver and of finite element based modeling (FEM) and of FEM validation [9]-[10]. The nonlinear force analysis was carried out using this modeling method. An overview of this modeling is presented as follows:

1) Material nonlinearity: We have previously reported the nonlinear elastic model of a pig liver [9] and breast [5]. This model was constructed by the torsional creep test using a rheometer (AR-G2, TA-Instrument). A creep test was carried out for various stresses to investigate material nonlinear properties. In our previous work, the steady state of the step response following sufficient elapsed time exhibits the low-frequency characteristics described in (1). Nonlinear properties can be modeled using the quadric function of strain described in equation (2). The parameters of these equations, measured by the experiment, are shown in Table I.

$$G\frac{d^k\gamma}{dt^k}=\tau \tag{1}$$

$$G=\begin{cases} G_o & (\gamma<\gamma_0) \\ G_0(1+a(\gamma-\gamma_0)^2) & (\gamma>\gamma_0) \end{cases} \tag{2}$$

where G is the magnitude of stiffness, G_o is the viscoelastic modulus of the linear range, a_γ is the coefficient when the change of γ is the shear strain and γ_0 is the strain in which the characteristics of soft tissue change show nonlinearity.

2) Finite element modeling: We have previously reported our solution for the finite element model and have also provided specific descriptions of the development of this model [9]-[10]. As shown in Fig. 5, a model was constructed with a breast shape similar to that of the breast used in the experiment, which is explained in section A. The shape of the breast model was assumed to be 40 mm square. As a boundary condition, we set the dorsal side of the model as the fixed end simulating the effect of the sternum (we used a metal plate in the experiment). The mesh was developed using the Delaunay method, which involves dividing the object automatically into triangular elements, based on the outline of the target object. This is one of the most accepted methods because of the uniquely high reliability resulting from its geometric division. We created the two models with the same shape and mesh but having different material properties: one consisted of 70% mammary gland and 30% fat; the other consisted of 100% mammary gland and 0% fat. The configuration of mesh and each tissue is presented in Fig. 5.

3) Material properties: The stiffness parameter of the model was decided based on our previous work to measure the nonlinear elasticity of breast tissues [5]. Our previous work [9] revealed that there are large differences between the stiffness parameters of in vitro tissue and in vivo tissue. Considering the above, linear elasticity G_o was manually set to correspond with the experimental results shown in Fig.6. Meanwhile, the nonlinear elastic parameters a_γ and γ_0 were not changed for the evaluation by difference in nonlinear elasticity. Table I shows the parameters of each tissue.

4) Simulation conditions: Nodes at probe contact at the center of the upper surface were displaced along the Y-axis at a rate of 3.0 mm/s. Time-series data for probe displacement and the external force were collected during the simulation. The simulations were carried out for both models.

III. Results

Figure 6 presents the experimental results of the reaction force during the indentations. Both reaction forces at point A and B increased linearly in response to small displacements of the indentation probe. The slopes of force increase were at similar magnitudes. The reaction force at point B exhibits a nonlinear increase after 4 mm of probe displacement. Meanwhile the force at point A remained linear after approximately 8 mm of displacement.

Figure 6 also presents the simulation results of the reaction force. The tendency was the same as in the experimental results; a small difference in reaction force in the linear range in response to small displacement and a large difference in the reaction force in the nonlinear range in response to large

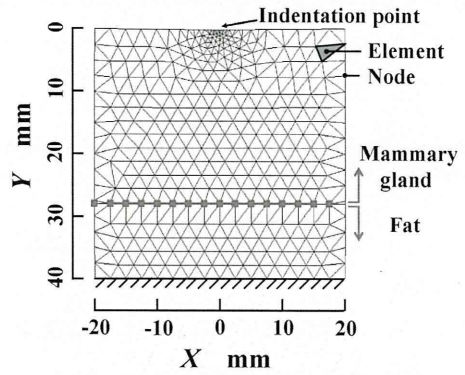

Fig.5. Boundary conditions of breast model mesh. The rear side of the model was set to be the fixed end.

TABLE I
PARAMETER OF EACH TISSUE OF THE BREAST MODEL

Tissue type	G_0 Pa	γ_0	a_γ
Fat	3.0×10^3	0.87	2.1
Mammary gland	4.8×10^3	0.44	2.1×10^1

displacement. The reaction force in the simulation was small in both nonlinear and linear ranges compared with the experimental result. The magnitude of nonlinearity in the simulation was also small compared with the experimental results.

IV. Discussion

1) Feasibility of our concept: There were small differences in the linear range in the reaction force during small displacements between the experimental and simulation results. On the other hand, this difference became large when the probe displacement became large and the reaction force became nonlinear. A small difference of reaction force may result in mischaracterization of tissue. Therefore, we suggest that it is preferable to identify tissue type by evaluating nonlinear elasticity rather than linear elasticity. These results support the feasibility of our concept to evaluate the nonlinear reaction force following large deformation of the breast.

2) Two dimensional analysis and model shape: we developed a 2D liver model and provided a 2D deformation simulation. It is acknowledged that a 3D model would provide more accurate results. However, an assumption, supported by related studies [11], was made that 2D simulation and manipulator movement would be sufficiently effective to enable accurate needle insertion. A comparative evaluation of 2D and 3D simulation will be undertaken in future work. The other limitation in our investigation is the shape of the model. We simulated the reaction force with a simplified structure.

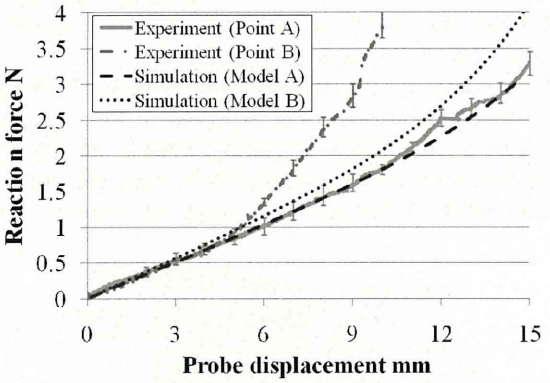

Fig.6. Experimental and simulation results of the reaction force (Average value of three experiments).

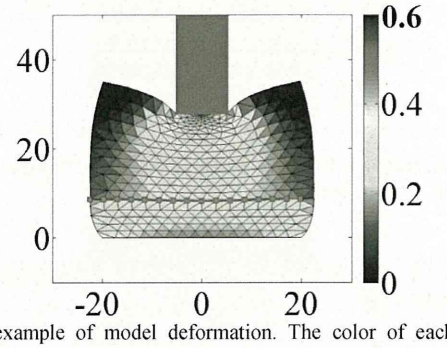

Fig.7. An example of model deformation. The color of each element represents the strain of the element.

The actual shape of the breast used in square breast model as the experiment was not square but a more complex structure. It is likely that the limitations of dimension and shape of the model result in the difference between the simulation and experimental results.

3) Tissue limitation: This article only covered mammary gland and fat as target tissues. The goal of our research is to characterize all the constituent breast tissues. Tissues such as muscle and tumor will be addressed in future work.

V. Summary And Future Work

We propose the palpation diagnosis system based on the measurement of nonlinear elasticity to identify the location of each breast tissue. Here, we have presented the basic concept of our study with preliminary experiment and simulation. More specifically, we performed an experiment to measure the nonlinear response of reaction force using the breast of a goat. In addition, we also simulated the reaction force using a nonlinear biomechanical simulation with several tissue types. Large differences in reaction force occur only in the nonlinear range in both experimental and simulation situations. Our results confirmed the feasibility of our concept.

In future work, we will examine the reaction force with a 3D breast model. We will perform an investigation that will include breast muscle and tumor. From these results, we will develop a palpation system for tissue characterization.

References

[1] N. Famaey, J. V. Sloten, "Soft tissue modelling for applications in virtual surgery and surgical robotics", *J. Comp. Meth. Biomech. and Bio-med. Eng.*, vol. 11, no. 4, pp. 351-366, 2008.

[2] T. A. Krouskop, T. M. Wheeler, F. Kallel, B. S. Garra, T. Hall, "Elastic moduli of breast and prostate tissues under compression", *Ultrason.. Imaging*, vol.20, pp. 260-274, 1998.

[3] P. S. Wellman, "Breast Tissue Stiffness in Compression is Correlated to Histological Diagnosis", PhD dissertation, Harvard University, USA, 1999.

[4] A Samani, "Measurement of the hyperelastic properties of 44 pathological ex vivo breast tissue samples", Institute of Physics and Engineering in Medicine, vol. 54, pp. 2557–2569, 2009

[5] M. Tsukune, .Y Kobayashi, T. Hoshi, T. Miyashita and M.G. Fujie, Member," Measuring the nonlinear elastic properties of soft tissues that compose breast and comparison of measurement results", in *33rd Annu. Int. Conf. IEEE EMBS*, accepted for publication, 2011.

[6] T. J. Hall, A. A. Oberai, P. E. Barbone, A. M. Sommer, N. H. Gokhale S. Goenezen and J. Jiang, "Elastic Nonlinearity Imaging", 31st Annual International Conference of the IEEE EMBS, pp. 1967-1970

[7] N. Nitta and T. Shiina, "Estimation of Nonlinear Elasticity Parameter of Tissues by Ultrasound", *Jpn. J. Appl. Phys.* vol. 41 pp. 3572–3578, 2002

[8] Z. G. Wang, Y. Liu, G. Wang, and L. Z. Sun, "Elastography Method for Reconstruction of Nonlinear Breast Tissue Properties", Int. J. Biomed. Imag., vol. 2009, Article ID 406854, 9 pages doi:10.1155/2009/406854

[9] Y. Kobayashi et al., " Development and validation of a viscoelastic and nonlinear liver model for needle insertion", International Journal of Computer Assisted Radiology and Surgery, Vol. 4(1), pp.53-63, 2009

[10] Y. Kobayashi et al., , "A Robotic Palpation-Based Needle Insertion Method for Diagnostic Biopsy and Treatment of Breast Cancer", in Proc. 2009 IEEE Int. Conf. Intelligent Robots and Systems, 2009, pp.5534-5539.

[11] S. P. DiMaio, and S. E. Salcudean "Needle insertion modeling and simulation," *IEEE Trans. Robot. Autom.*, vol. 19, no. 5, pp. 864–875, 2003.

Europace (2011) **13**, 1774–1780
doi:10.1093/europace/eur256

Prevalence and characteristics of idiopathic right ventricular outflow tract arrhythmias associated with J-waves

Yoshihiro Yamashina[1,2], Tetsuo Yagi[1]*, Akio Namekawa[1], Akihiko Ishida[1], Hirokazu Sato[1,2], Takashi Nakagawa[1], Manjirou Sakuramoto[1], Eiji Sato[1,2], and Tomoyuki Yambe[2]

[1]Division of Cardiology, Sendai City Hospital, Wakabayashi-ku, Shimizukouji3-1, Sendai, Japan; and [2]Department of Medical Engineering and Cardiology, Institute of Development, Aging and Cancer, Tohoku University, Sendai, Japan

Received 24 May 2011; accepted after revision 6 July 2011; online publish-ahead-of-print 15 August 2011

Aim The arrhythmogenic relationship between the presence of J-waves during sinus rhythm and idiopathic ventricular tachycardia (VT) or pre-mature ventricular contractions (PVCs) originating from the right ventricular outflow tract (RVOT) has not been reported. The aim of this study was to investigate the prevalence and characteristics of idiopathic RVOT–VT/PVCs associated with J-waves.

Methods and results The study enrolled 138 consecutive idiopathic RVOT–VT/PVC patients undergoing radiofrequency catheter ablation (RFCA) and 276 age- and gender-matched control subjects. The prevalence of J-waves was assessed in each cohort, and the clinical and electrophysiological data were compared between the RVOT–VT/PVC patients with J-waves (J-RVOT–VT/PVC group) and those without (non-J-RVOT–VT/PVC group). J-waves were more common among patients with idiopathic RVOT–VT/PVCs than among the matched control subjects (40 vs. 16% $P < 0.001$). The J-RVOT–VT/PVC group had a higher incidence of sustained VT (25 vs. 5%, $P < 0.01$), shorter VT cycle length (302 ± 57 vs. 351 ± 58 ms, $P < 0.001$), and more episodes of syncope (25 vs. 2%, $P < 0.001$) than did the non-J-RVOT–VT/PVC group. However, no patients demonstrated any ventricular fibrillation (VF) or cardiac sudden death in either group.

Conclusions There was a high prevalence of J-waves in the idiopathic RVOT–VT/PVC patients referred for RFCA. Although patients with idiopathic RVOT arrhythmias associated with J-waves might have a more enhanced arrhythmogenicity than those without J-waves, the significance of those J-waves was limited in terms of the prognosis and VF.

Keywords J-waves • Pre-mature ventricular contraction • Right ventricular outflow tract • Ventricular tachycardia

Introduction

Recently, the presence of J-waves (notching or slurring after the QRS complex during sinus rhythm) in the inferior-lateral leads of the 12-lead electrocardiogram (ECG) has been reported to be associated with ventricular arrhythmias.[1–8] In the initial case-control study describing an idiopathic ventricular fibrillation (VF) associated with J-waves (J-wave syndrome) published by Haïssaguerre *et al.*[1] when pre-mature ventricular contractions (PVCs) were present and documented in a J-wave syndrome patient, their origin was from the area of the J-waves and it was considered as a strong argument to link idiopathic VF and J-waves in the inferior-lateral region. To the best of our knowledge the arrhythmogenic relationship between idiopathic ventricular tachycardia (VT)/PVCs arising from the right ventricular outflow tract (RVOT), which are the most common type of ventricular arrhythmias in structurally normal hearts,[9,10] and J-waves has not been previously reported. However, we actually encountered a case of unexpected sudden death due to VF while observing for J-waves and suspected idiopathic RVOT–PVCs (*Figure 1*).[11] Another case report also described an

* Corresponding author. Tel: +81 022 266 7111; fax: +81 022 211 8972, Email: tetsuo.yagi@nifty.com

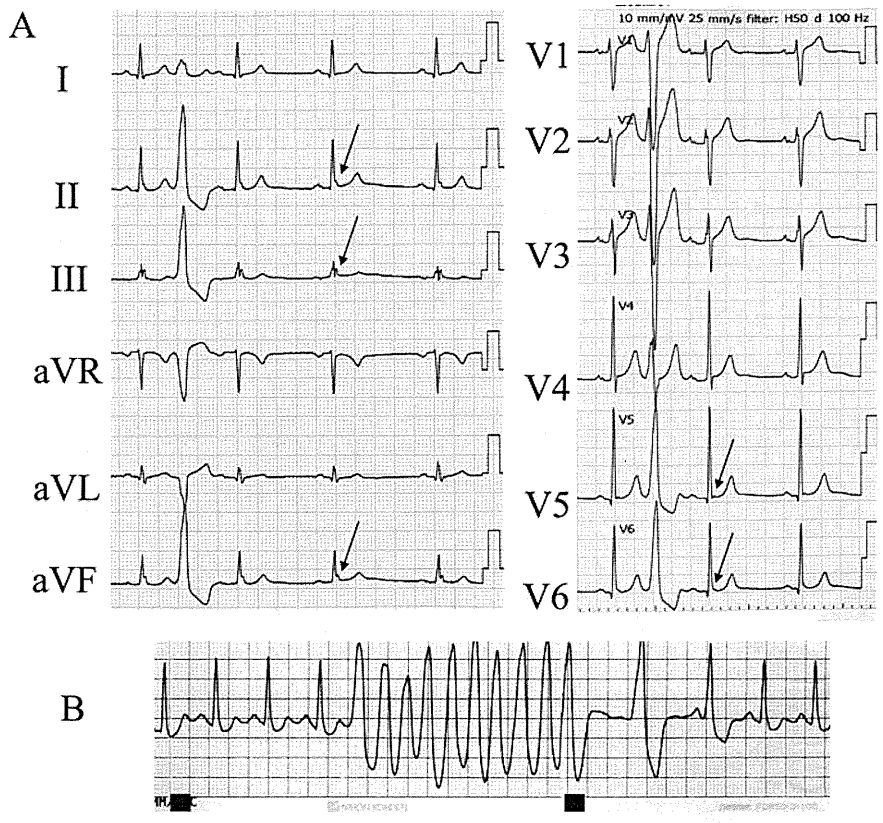

Figure 1 (*A*) A 12-lead electrocardiogram in a 45-year-old male who suffered from sudden cardiac death due to ventricular fibrillation.[11] This electrocardiogram was recorded incidentally 1 month before his sudden death. He had no evidence of any cardiac disease. The electrocardiogram demonstrates J-waves (arrow) in the inferior leads and V5–6 during sinus rhythm and pre-mature ventricular contractions with a left bundle branch block and inferior-axis deviation. (*B*) The monitored electrocardiogram in the same patient after the resuscitation. A rapid non-sustained ventricular tachycardia was observed (cycle length = 210 ms). Unfortunately, we could not perform an electrophysiological evaluation or radiofrequency catheter ablation for this patient because he died due to hypoxic encephalopathy 5 days after the resuscitation. Adapted with permission from the publisher of the *Journal of Sendai City Hospital* (in Japanese).

exercise-induced sustained RVOT-type VT associated with J point elevation in the inferior leads in a patient without apparent heart disease.[12] It is unknown as to whether or not the presence of J-waves affects the arrhythmogenicity of idiopathic RVOT–VT/PVCs. The purpose of this study was to investigate the prevalence and characteristics of idiopathic RVOT–VT/PVCs associated with J-waves.

Methods

Study population

The study was approved by the institutional review board. We reviewed the database of 138 consecutive patients (mean age 44 ± 15 years, 45 males) in whom radiofrequency catheter ablation (RFCA) was conducted for the treatment of idiopathic RVOT–VT/PVCs at our institute. No patients had any structural heart disease. Patients with coronary artery disease, any cardiomyopathies including arrhythmogenic right ventricular cardiomyopathy/dysplasia (ARVC/D),[13] Brugada syndrome,[14] catecholaminergic polymorphic ventricular tachycardia,[15] or long or short QT syndrome[4,16] were excluded. The control group consisted of 276 age- and gender-matched healthy subjects who were selected from among 7110 subjects who had routine health care examinations (12-leads ECG, blood test, chest X-ray film, and physical examinations) at our hospital health care centre between 2007 and 2009. The subjects with an abnormal 12-lead ECG (i.e. any arrhythmias, wide QRS complex, ST-segment elevation, T-wave inversion, QT interval abnormality, or Brugada-type ECG), blood test results, chest X-ray films, and physical examinations were excluded.

Definition of J-waves and analysis of the electrocardiogram parameters

The presence of J-waves during sinus rhythm (SR) was investigated in all the patients and control subjects. In the study patients, a 12-lead ECG was recorded after withdrawal of all antiarrhythmic drugs for at least five half-lives both 1–3 days before and 1–3 days after the RFCA. To blind the ECG interpreters to the patient grouping and patient information, all tracings were scanned and coded. Segments showing extra-systoles were not used. All scanned ECGs were analysed by two independent cardiologists in a random order and any controversial interpretations were re-discussed with a third observer. As previously described,[1–8,17–19] the J-waves were defined as an

elevation of the J point noted as either a QRS slurring or notching of ≥0.1 mV in ≥2 contiguous leads in the inferior leads (II, III, aVF), or a lateral (I, aVL, V4–V6) distribution (*Figures 1–3*). Other ECG parameters, including the PR interval, QRS duration, and QT interval corrected for the heart rate (QTc) during stable SR at baseline were measured in lead V2. The QTc interval was calculated after a correction for the heart rate with Bazett's formula.

Clinically, documented ventricular arrhythmias recorded by Holter recordings or ECG monitoring in the idiopathic RVOT–VT/PVC patients were analysed in terms of the coupling interval of the VT/PVCs (ms), tachycardia CL (ms), and form of the ventricular arrhythmias. The form of the ventricular arrhythmias was divided into the following criteria: (i) PVCs were defined as isolated or two consecutive ectopic ventricular beats, (ii) non-sustained VT was defined as >3 consecutive beats and which terminated spontaneously within 30 s, (iii) sustained VT was defined as VT lasting ≥30 s, and (iv) VF was defined as a polymorphic ventricular tachyarrhythmia with haemodynamic decompensation requiring direct cardioversion for termination.

Comparison between idiopathic right ventricular outflow tract-ventricular tachycardia/pre-mature ventricular contractions patients with and without J-waves

Based on the presence or absence of J-waves during SR in the 12-lead ECG before the RFCA, the idiopathic RVOT–VT/PVC patients were divided into two groups: the J-RVOT–VT/PVC group and non-J-RVOT–VT/PVC group. The patients' clinical characteristics, ECG parameters during both SR and RVOT–VT/PVCs, data from electro-physiological study, outcome of the RFCA, J-waves' appearance after the RFCA, and the follow-up data were compared between the two groups.

Statistical analysis

Continuous variables were expressed as the mean ± SD, and categorical variables were presented as the number and percent in each group. The prevalence of J-waves between the idiopathic RVOT–VT/PVC patients and control subjects was assessed by a conditional logistic regression analysis. A comparison of the continuous variables between the J-RVOT–VT/PVC group and non-J-RVOT–VT/PVC group was drawn by means of a Student's *t*-test. Categorical variables were compared using a χ^2 analysis with a Yates' correction if necessary. A *P* value <0.05 was considered significant (two-tailed).

Results

Prevalence of J-waves

Among the total of 138 RVOT–VT/PVC patients, six patients (four males) were excluded from the following analysis because of other coexisting ECG abnormalities [atrial fibrillation (1), second-degree atrio-ventricular block (1), sick sinus syndrome (1), and right bundle branch block (3)]. Another four patients (three males) demonstrated a J point elevation in the right pre-cordial leads (V1-3). Those four patients were also excluded from the following analysis in order to avoid any potential Brugada syndrome or ARVC/D.

J-waves were more common in the idiopathic RVOT–VT/PVC patients than among the matched control subjects [$n = 56$ (40) vs. $n = 46$ (16%), the odds ratio (OR) = 3.32, 95% confidence interval (CI) = 2.09–5.28, $P < 0.001$].

Comparison of the clinical, electrocardiographic, and electrophysiological characteristics between the J-right ventricular outflow tract-ventricular tachycardia/pre-mature ventricular contractions group and non-J-right ventricular outflow tract-ventricular tachycardia/pre-mature ventricular contractions group

Table 1 shows the comparison of the clinical parameters between the J-RVOT–VT/PVC group and non-J-RVOT–VT/PVC group. The patients in the two groups were of a similar age and gender. Prior episodes of syncope were more frequent in the J-RVOT–VT/PVC group than in the Non-J-RVOT–VT/PVC group (25 vs. 2% $P < 0.001$). The comparisons of the clinical ECG characteristics between the two groups are shown in *Table 2*. Isolated PVCs were a more common finding in the non-J-RVOT–VT/PVC group (23 vs. 47% $P < 0.01$). On the other hand, sustained VT was documented more frequently in the J-RVOT–VT/PVC group than in the non-J-RVOT–VT/PVC group (25 vs. 5% $P < 0.01$) (*Figure 2*). We could not document any VF in any of the patients. The coupling intervals of the initiating VT or PVCs did not differ between the two groups. However, the CL of the spontaneous VT was much shorter in the J-RVOT–VT/PVC group than in the non-J-RVOT–VT/PVC group (302 ± 57 vs. 351 ± 58 ms, $P < 0.001$) (*Figure 3*). The heart rate, PR interval, QRS duration, and QTc during SR did not differ statistically.

In all patients, no VF was induced by programmed electrical stimulation, and endocardial mapping represented no local abnormal electrograms, including fragmented or delayed potentials. Although four patients in the J-RVOT–VT/PVC group required rapid ventricular electrical stimulation to induce their clinical RVOT–VT/PVCs (*Figure 2A*), we could not demonstrate any electro-physiological evidence of a reentrant VT mechanism. No one in the non-J-RVOT–VT/PVC group needed any electrical ventricular stimulation to induce their clinical VT/PVCs during the electrophysiological study. No significant difference was observed regarding the success rate of the RFCA between the two groups (*Table 2*). After the RFCA, no J-waves were recorded in five patients in the J-RVOT–VT/PVC group. No one in the non-J-RVOT–VT/PVC group developed any J-waves after the RFCA.

The follow-up data were obtained in all patients in the J-RVOT–VT/PVC group and in 69 (95%) in the non-J-RVOT–VT/PVC group at our outpatient clinic. Three patients in the non-J-RVOT–VT/PVC group were referred to other institutions. No deaths were observed in any of the patients during the follow-up period (median of 12 months, interquartile range 4–25 months).

Discussion

To the best of our knowledge this is the first report showing the relationship between J-waves and idiopathic RVOT–VT/PVCs. The main findings in this study were as follows: (i) The prevalence of J-waves was 40% in the idiopathic RVOT–VT/PVC patients referred for RFCA in our institution, which was higher compared

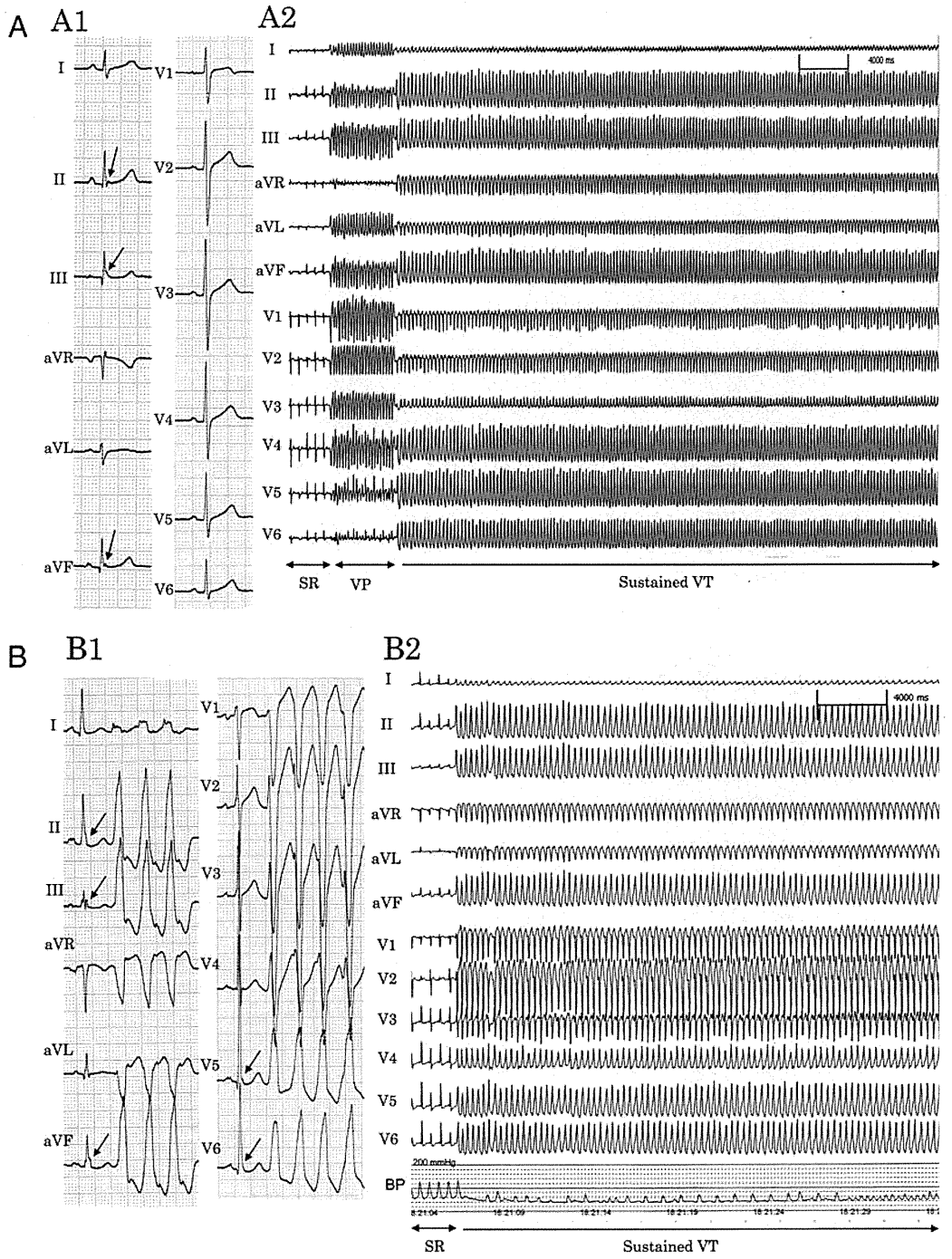

Figure 2 Two representative male patients with idiopathic right ventricular outflow tract-ventricular tachycardia associated with J-waves. (*A*) The 12-lead electrocardiograms in a 53-year-old male. (A1) The 12-lead electrocardiogram demonstrates the J-waves (QRS notching) in the inferior leads (arrow) during sinus rhythm. (A2) The 12-lead electrocardiogram during an electrophysiological study. The sustained ventricular tachycardia was induced by rapid ventricular pacing. (*B*) The 12-lead electrocardiograms in a 56-year-old male who suffered from repetitive syncopal episodes. (B1) The 12-lead electrocardiogram demonstrates the J-waves (QRS notching in the inferior leads and QRS slurring in V5–6: arrow), and non-sustained ventricular tachycardia with a left bundle branch block and inferior-axis deviation. (B2) The 12-lead electrocardiogram during an electrophysiological study. The sustained ventricular tachycardia appeared spontaneously with rapid lowering of the blood pressure. Radiofrequency catheter ablation of the ventricular tachycardia origin located in the right ventricular outflow tract completely eliminated the ventricular tachycardia in both patients.

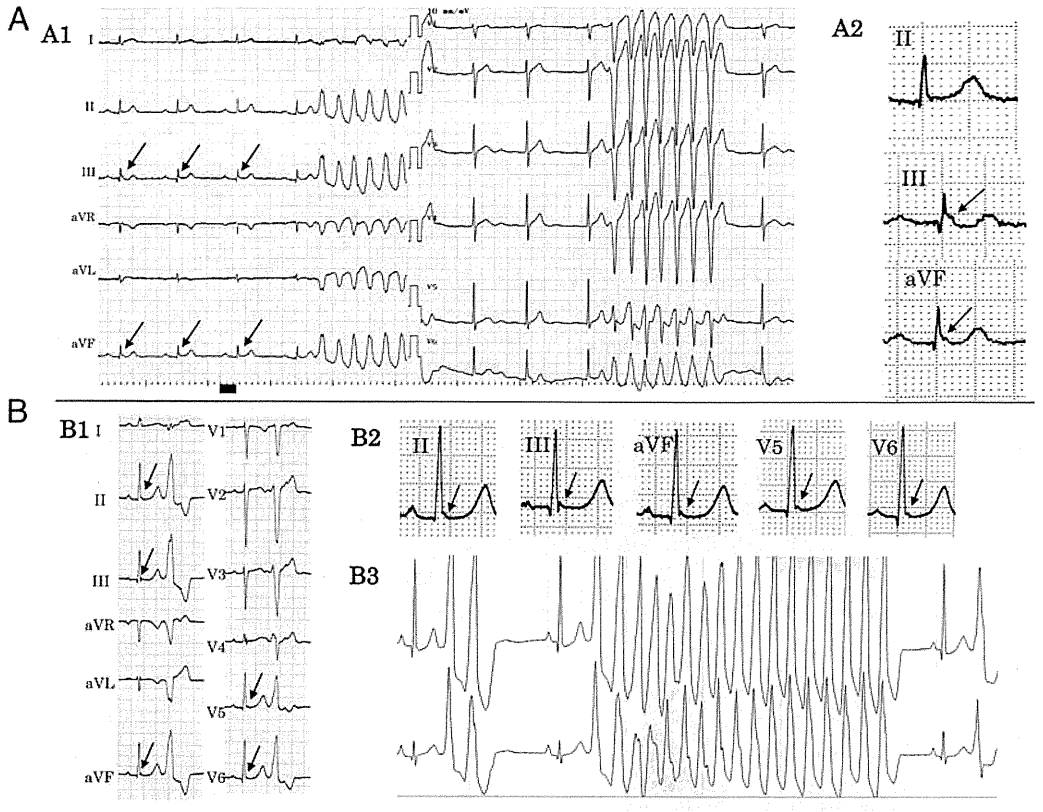

Figure 3 Two representative female patients in the J-right ventricular outflow tract-ventricular tachycardia/pre-mature ventricular contraction group. (*A*) A 42-year-old female. A1 and A2 show the baseline 12-lead electrocardiograms. The electrocardiogram demonstrates the J-waves (QRS notching) in the inferior leads (arrow) during sinus rhythm and rapid non-sustained ventricular tachycardia (cycle length=220 ms). (*B*) A 16-year-old female. B1 and B2 show the baseline electrocardiograms. The 12-lead electrocardiogram demonstrates the J-waves (QRS notching) in the inferior leads and in V5–6 (arrow) during sinus rhythm. (B3) The holter electrocardiogram in the same patient shows a very rapid non-sustained ventricular tachycardia (cycle length = 190 ms). Radiofrequency catheter ablation of the ventricular tachycardia origin in the right ventricular outflow tract completely eliminated the ventricular tachycardia in both patients.

Table 1 Comparison of the clinical characteristics between the J-right ventricular outflow tract–ventricular tachycardia/pre-mature ventricular contraction group and non-J-right ventricular outflow tract–ventricular tachycardia/pre-mature ventricular contraction group

Variables	J-RVOT–VT/PVC group ($n = 56$)	Non-J-RVOT–VT/PVC group ($n = 72$)	*P* value
Age (year)	44 ± 15	43 ± 15	0.32
Male gender	35% ($n = 20$)	25% ($n = 18$)	0.18
FH	5% ($n = 3$)	1% ($n = 1$)	0.44
Syncope	25% ($n = 14$)	2% ($n = 2$)	<0.001
Pre-syncope	14% ($n = 8$)	13% ($n = 10$)	0.84

FH, family history of sudden death.

with that in the healthy matched control subjects, (ii) idiopathic RVOT–VT/PVC patients associated with J-waves had a significantly higher incidence of sustained VT, shorter VT CL, and more episodes of syncope than did the idiopathic RVOT–VT/PVC patients without J-waves, and (iii) No patients demonstrated any VF or sudden death in the clinical course.

The presence of J-waves is a common ECG finding. It is present in 2–13% of the general population and usually is considered as a normal variant due to its benign long-term prognosis.[1–4,8,17] However, recent clinical studies have reported an association between J-waves and idiopathic VF.[1–3] Some studies have also suggested a high prevalence and arrhythmogenic significance of J-waves in various underlying arrhythmogenic situations (i.e. short QT syndrome,[4] ARVD/C,[5] chronic coronary artery disease,[7] and Wolff–Parkinson-White syndrome[18]). On the other hand, idiopathic RVOT–VT/PVCs are the most common and usually are benign ventricular arrhythmias in patients without structual heart disease.[9,10] It remains unknown as to whether or not the presence of J-waves affects the arrhythmogenicity of idiopathic RVOT–VT/

Table 2 Comparison of the clinical electrocardiogram characteristics and ablation outcome between the J-right ventricular outflow tract–ventricular tachycardia/pre-mature ventricular contraction group and non-J-right ventricular outflow tract–ventricular tachycardia/pre-mature ventricular contraction group

Variables	J-RVOT–VT/PVC group ($n = 56$)	Non-J-RVOT–VT/PVC group ($n = 72$)	*P* value
Presenting arrhythmia			
PVCs	23% ($n = 13$)	47% ($n = 34$)	<0.01
Non-sustained VT	51% ($n = 29$)	47% ($n = 34$)	0.60
Sustained VT	25% ($n = 14$)	5% ($n = 4$)	<0.01
VF	0% ($n = 0$)	0% ($n = 0$)	
CI of VT/PVCs (ms)	444 ± 89	452 ± 85	0.61
CL of VT (ms)	302 ± 57 ($n = 43$)	351 ± 58 ($n = 38$)	<0.001
Parameters during sinus rhythm			
Heart rate (bpm)	65 ± 8	66 ± 12	0.31
QRS duration (ms)	54 ± 8	53 ± 9	0.62
PR interval (ms)	177 ± 20	177 ± 20	0.92
QTc (ms)	397 ± 23	399 ± 22	0.71
Successful RFCA	94% ($n = 53$)	90% ($n = 65$)	0.56

CI, coupling interval; CL, cycle length; PVCs, pre-mature ventricular contractions; QTc, QT interval corrected for heart rate with Bazett's formula; RFCA, radiofrequency catheter ablation; VF, ventricular fibrillation; VT, ventricular tachycardia.

PVCs. In the present study the prevalence of J-waves was surprisingly high (40%) in the idiopathic RVOT–VT/PVC patients referred for RFCA. We speculate that this high percentage of J-waves may represent an enhanced arrhythmogenicity in these patients. Patients with symptomatic and risky idiopathic RVOT–VT/PVCs are more likely to be referred for RFCA. Indeed, there was an intriguing correlation between the idiopathic RVOT–VT/PVC patients and J-waves with regard to sustained VT, short VT CL, and syncope.

On the other hand, we could not detect any documented VF in the present study cohort. This result is not surprising because idiopathic RVOT–VT/PVCs are usually benign.[9,10] Our data suggest that the significance of J-waves in idiopathic RVOT–VT/PVC patients may be limited in terms of the overall prognosis and occurrence of VF. However, some recent reports have shown that idiopathic RVOT–VT/PVCs occasionally cause VF or sudden death ('malignant' idiopathic RVOT–VT/PVCs).[20,21] The mechanism of the malignant form of idiopathic RVOT–VT/PVCs is unknown. Moreover, the electrophysiological mechanisms of the arrhythmogenesis related to J-waves have not been established. There is controversy over whether the pathogenesis of J-waves is related to an early ventricular repolarization abnormality or ventricular depolarization abnormality.[3] In experimental studies, Antzelevitch and co-workers[22–24] proposed that an epicardial–endocardial heterogeneity of the repolarization was responsible for J-waves observed in patients with idiopathic VF as well as Brugada syndrome. Further, delayed after depolarizations (DADs) and triggered activity are believed to be the underlying mechanism of idiopathic RVOT–VT/PVCs.[10,11] There have been no clinical studies explaining the direct link between the increased dispersion of ventricular repolarization and the DAD-induced triggered activity. However, Antzelevitch and co-workers[25,26] demonstrated that DAD-induced triggered beats originated in the epicardium, leading to a reversal of the direction of the activation (from the epicardium to the endocardium instead the normal endocardial to epicardial activation), leads to a dramatic increase in the transmural dispersion of the repolarization. They speculated that DADs originating from the RVOT-epicardium not only initiate VT but also create the substrate for reentry by increasing the dispersion of the ventricular repolarization.[25,26] Although previous studies reporting 'malignant' idiopathic RVOT–VT/PVCs did not mention about the presence of J-waves in their patient series, some clinical features are overlapping between the 'malignant' idiopathic RVOT–VT/PVCs reported previously[20] and the idiopathic RVOT–VT/PVCs associated with J-waves in the present study (i.e. shorter tachycardia CL and more episodes of syncope). We speculate that the presence of J-waves may reflect a potential propensity of ventricular proarrhythmias even in idiopathic RVOT–VT/PVCs patients. Although the proposed mechanism of sudden cardiac arrest associated with J-waves would suggest that these patients should present with VF, the exact mechanisms are yet to be elucidated. Some investigators have described an association between monomorphic VT and the presence of J-waves.[6–8,12] Numerous reports have been published on patients with Brugada syndrome who have presented with monomorphic VT.[27–29] The mechanisms and clinical implications of coexisting monomorphic VT and VF in Brugada syndrome also have not been clarified. Further clinical and experimental studies are needed to clarify the significance and risk of idiopathic VT/PVCs associated with underlying proarrhythmic situations such as J-waves in the inferior-lateral leads or Brugada pattern ECGs.

Study limitations

The present study had several limitations. First, this study was a single-centre, retrospective analysis. A further prospective evaluation is needed in a larger study population. Secondly, the present study cohort had a potential referral bias, because the patients with symptomatic and high-risk RVOT–VT/PVCs are more likely to be referred for RFCA, whereas asymptomatic patients are more likely to be treated conservatively. Therefore, we could not confirm the true prevalence of J-waves in the overall idiopathic RVOT–VT/PVC patients with this study design. Thirdly, all patients underwent a 12-lead ECG at least twice before and after the RFCA; however, the day-to-day variability in the ECG patterns should have been evaluated using more frequent ECG recordings. Fourthly, all patients and control subjects in the present study were Japanese. We could not analyse the relationship between the prevalence of J-waves and the genetic/ethnic differences. Very recently, an epidemiologic study in the Japanese population revealed that J-waves were common ECG findings, yielding a positive rate of 23.9% during the follow-up.[19] It is possible that the high prevalence of J-waves in the present study reflected a genetic characteristic.

Conclusions

There was a high prevalence of J-waves in the idiopathic RVOT–VT/PVC patients referred for RFCA. Although patients with idiopathic RVOT arrhythmias associated with J-waves might have a more enhanced arrhythmogenicity than those without J-waves, the significance of those J-waves was limited in terms of the prognosis and VF. Further clinical and experimental studies are needed to clarify the clinical and electrophysiological relationship between the J-waves and idiopathic RVOT–VT/PVCs.

Conflict of interest: none declared.

References

1. Haïssaguerre M, Derval N, Sacher F, Jesel L, Deisenhofer I, de Roy L *et al.* Sudden cardiac arrest associated with early repolarization. *N Engl J Med* 2008;**358**:2016–23.
2. Rosso R, Kogan E, Belhassen B, Rozovski U, Scheinman MM, Zeltser D *et al.* J-point elevation in survivors of primary ventricular fibrillation and matched control subjects: incidence and clinical significance. *J Am Coll Cardiol* 2008;**52**:1231–8.
3. Abe A, Ikeda T, Tsukada T, Ishiguro H, Miwa Y, Miyakoshi M *et al.* Circadian variation of late potentials in idiopathic ventricular fibrillation associated with J waves: insights into alternative pathophysiology and risk stratification. *Heart Rhythm* 2010;**7**:675–82.
4. Watanabe H, Makiyama T, Koyama T, Kannankeril PJ, Seto S, Okamura K *et al.* High prevalence of early repolarization in short QT syndrome. *Heart Rhythm* 2010;**7**:647–52.
5. Peters S, Selbig D. Early repolarization phenomenon in arrhythmogenic right ventricular dysplasia-cardiomyopathy and sudden cardiac arrest due to ventricular fibrillation. *Europace* 2008;**10**:1447–9.
6. Merchant FM, Noseworthy PA, Weiner RB, Singh SM, Ruskin JN, Reddy VY. Ability of terminal QRS notching to distinguish benign from malignant electrocardiographic forms of early repolarization. *Am J Cardiol* 2009;**104**:1402–6.
7. Patel RB, Ng J, Reddy V, Chokshi M, Parikh K, Subacius H *et al.* Early repolarization associated with ventricular arrhythmias in patients with chronic coronary artery disease. *Circ Arrhythm Electrophysiol* 2010;**3**:489–95.
8. Cappato R, Furlanello F, Giovinazzo V, Infusino T, Lupo P, Pittalis M *et al.* J wave, QRS slurring, and ST elevation in athletes with cardiac arrest in the absence of heart disease: marker of risk or innocent bystander? *Circ Arrhythm Electrophysiol* 2010;**3**:305–11.
9. Zipes DP, Camm AJ, Borggrefe M, Buxton AE, Chaitman B, Fromer M *et al.* ACC/AHA/ESC 2006 guidelines for management of patients with ventricular arrhythmias and the prevention of sudden cardiac death: a report of the American College of Cardiology/American Heart Association Task Force and the European Society of Cardiology Committee for Practice Guidelines. *Europace* 2006;**8**:746–837.
10. Ghanbari H, Schmidt M, Machado C, Daccarett M. Catheter ablation of ventricular tachycardia in structurally normal hearts. *Expert Rev Cardiovasc Ther* 2010;**8**:651–61.
11. Yamashina Y, Yagi T, Namekawa A, Ishida A, Sato H, Nakagawa T *et al.* A case of sudden cardiac death during observation for idiopathic left bundle branch block and inferior axis deviation type premature ventricular contractions and J waves in inferior leads. *J Sendai City Hosp* 2010;**30**:71–4. (in Japanese).
12. Ozeke O, Aras D, Celenk MK, Deveci B, Yildiz A, Topaloglu S *et al.* Exercise-induced ventricular tachycardia associated with J point ST-segment elevation in inferior leads in a patient without apparent heart disease: a variant form of Brugada syndrome? *J Electrocardiol* 2006;**39**:409–12.
13. Cox MG, van der Smagt JJ, Noorman M. Arrhythmogenic right ventricular dysplasia/cardiomyopathy diagnostic task force criteria: impact of new task force criteria. *Circ Arrhythm Electrophysiol* 2010;**3**:126–33.
14. Brugada P, Brugada J. Right bundle branch block, persistent ST segment elevation and sudden cardiac death: a distinct clinical and electrocardiographic syndrome. A multicenter report. *J Am Coll Cardiol* 1992;**20**:1391–6.
15. Leenhardt A, Lucet V, Denjoy I, Grau F, Ngoc DD, Coumel P. Catecholaminergic polymorphic ventricular tachycardia in children. A 7-year follow-up of 21 patients. *Circulation* 1995;**91**:1512–9.
16. Moss AJ, Schwartz PJ, Crampton RS, Locati E, Carleen E. The long QT syndrome: a prospective international study. *Circulation* 1985;**71**:17–21.
17. Sinner MF, Reinhard W, Müller M, Beckmann BM, Martens E, Perz S *et al.* Association of early repolarization pattern on ECG with risk of cardiac and all-cause mortality: a population-based prospective cohort study (MONICA/KORA). *PLoS Med* 2010;**7**:e1000314.
18. Mizumaki K, Nishida K, Iwamoto J, Nakatani Y, Yamaguchi Y, Sakamoto T *et al.* Early repolarization in Wolff–Parkinson-White syndrome: prevalence and clinical significance. *Europace* 2011;**13**:1195–1200.
19. Daisuke Haruta, Kiyotaka Matsuo, Akira Tsuneto, Shinichiro Ichimaru, Ayumi Hida, Nobuko Sera *et al.* Incidence and prognostic value of early repolarization pattern in the 12-lead electrocardiogram. *Circulation* 2011;**123**:2931–7.
20. Noda T, Shimizu W, Taguchi A, Aiba T, Satomi K, Suyama K *et al.* Malignant entity of idiopathic ventricular fibrillation and polymorphic ventricular tachycardia initiated by premature extrasystoles originating from the right ventricular outflow tract. *J Am Coll Cardiol* 2005;**46**:1288–94.
21. Viskin S, Rosso R, Rogowski O, Belhassen B. The 'short-coupled' variant of right ventricular outflow ventricular tachycardia: a not-so-benign form of benign ventricular tachycardia? *J Cardiovasc Electrophysiol* 2005;**16**:912–6.
22. Gussak I, Antzelevitch C. Early repolarization syndrome: clinical characteristics and possible cellular and ionic mechanisms. *J Electrocardiol* 2000;**33**:299–309.
23. Yan GX, Antzelevitch C. Cellular basis for the Brugada syndrome and other mechanisms of arrhythmogenesis associated with ST-segment elevation. *Circulation* 1999;**100**:1660–6.
24. Yan GX, Antzelevitch C. Cellular basis for the electrocardiographic J wave. *Circulation* 1996;**93**:372–9.
25. Fish JM, Di Diego JM, Nesterenko V, Antzelevitch C. Epicardial activation of left ventricular wall prolongs QT interval and transmural dispersion of repolarization: implications for biventricular pacing. *Circulation* 2004;**109**:2136–42.
26. Viskin S, Antzelevitch C. The cardiologists' worst nightmare sudden death from 'benign' ventricular arrhythmias. *J Am Coll Cardiol* 2005;**46**:1295–7.
27. Shimada M, Miyazaki T, Miyoshi S, Soejima K, Hori S, Mitamura H *et al.* Sustained monomorphic ventricular tachycardia in a patient with Brugada syndrome. *Jpn Circ J* 1996;**60**:364–70.
28. Dinckal MH, Davutoglu V, Akdemir I, Soydinc S, Kirilmaz A, Aksoy M. Incessant monomorphic ventricular tachycardia during febrile illness in a patient with Brugada syndrome: fatal electrical storm. *Europace* 2003;**5**:257–61.
29. Chinushi M, Furushima H, Hosaka Y, Izumi D, Aizawa Y. Ventricular fibrillation and ventricular tachycardia triggered by late-coupled ventricular extrasystoles in a Brugada syndrome patient. *Pacing Clin Electrophysiol* 2011;**34**:e1–5.

Hindawi Publishing Corporation
Evidence-Based Complementary and Alternative Medicine
Volume 2011, Article ID 157090, 6 pages
doi:10.1155/2011/157090

Research Article

Short-Term Effects of Acupuncture on Open-Angle Glaucoma in Retrobulbar Circulation: Additional Therapy to Standard Medication

Shin Takayama,[1] Takashi Seki,[1] Toru Nakazawa,[2] Naoko Aizawa,[2] Seri Takahashi,[2] Masashi Watanabe,[1] Masayuki Izumi,[1] Soichiro Kaneko,[1] Tetsuharu Kamiya,[1] Ayane Matsuda,[1] Akiko Kikuchi,[1] Tomoyuki Yambe,[3] Makoto Yoshizawa,[4] Shin-ichi Nitta,[3] and Nobuo Yaegashi[1]

[1] *Department of Traditional Asian Medicine, Graduate School of Medicine, Tohoku University, 1-1 Seiryo-machi, Aoba-ku, Sendai, Miyagi 980-8574, Japan*
[2] *Department of Ophthalmology and Visual Science, Graduate School of Medicine, Tohoku University, Sendai 980-8574, Japan*
[3] *Institute of Development, Aging and Cancer, Tohoku University, Sendai 980-8575, Japan*
[4] *Research Division on Advanced Information Technology, Cyberscience Center, Tohoku University, Japan*

Correspondence should be addressed to Takashi Seki, t-seki@m.tohoku.ac.jp

Received 29 October 2010; Revised 7 December 2010; Accepted 11 January 2011

Background. The relation between glaucoma and retrobulbar circulation in the prognosis has been indicated. *Purpose.* To investigate the effects of acupuncture on retrobulbar circulation in open-angle glaucoma (OAG) patients. *Methods.* Eleven OAG patients (20 eyes with OAG) who were treated by topical antiglaucoma medications for at least 3 months were enrolled. Acupuncture was performed once at acupoints BL2, M-HN9, ST2, ST36, SP6, KI3, LR3, GB20, BL18, and BL23 bilaterally. Retrobulbar circulation was measured with color Doppler imaging, and intraocular pressure (IOP) was also measured at rest and one hour after rest or before and after acupuncture. *Results.* The Δ value of the resistive index in the short posterior ciliary artery ($P < .01$) and the Δ value of IOP ($P < .01$) were decreased significantly by acupuncture compared with no acupuncture treatment. *Conclusions.* Acupuncture can improve the retrobulbar circulation and IOP, which may indicate the efficacy of acupuncture for OAG.

1. Introduction

Glaucoma is one of the causes of blindness [1] and the Tajimi Study showed that the prevalence of primary open-angle glaucoma (OAG) was 3.9% in Japan [2]. The main treatment strategy of glaucoma is to control the intraocular pressure (IOP) [3]. Although IOP reduction is currently the main target for the treatment of glaucoma, treatment modalities that enhance retrobulbar hemodynamics in addition to reducing IOP may have a beneficial effect on the glaucoma therapy. It has been reported that glaucoma is associated with reduction in the blood flow velocity and elevation of the resistive index (RI) in the retrobulbar vessels [4–7]. It has also been reported that patients with OAG have impaired hemodynamics in ophthalmic circulation [8–10]. The impaired ocular circulation contributes to the progression of glaucomatous damage [11–13]. Therefore, new drugs or interventions that improve ocular hemodynamics may be preferable.

Recently, acupuncture has been widely applied to treat several conditions such as neck pain, shoulder pain, lumbar pain, headache, and hypertension in Asian and Western countries, and it has also been found to be effective for many conditions in several randomized trials [14–20]. Acupuncture has also been used for the treatment of ocular diseases, including glaucoma, in traditional Chinese medicine [21]. We have shown that acupuncture therapy added to the standard medication could affect the IOP level in eyes with normal-tension glaucoma [22], and several other studies have demonstrated that

acupuncture improves choroidal blood flow in the eye [23–25].

We have already reported that color Doppler imaging (CDI) by ultrasound is suitable for measuring the blood flow change in several organs during traditional Chinese medicine therapy [26–30]. The real-time and noninvasive hemodynamic measurement with CDI has been applied for measuring the retrobulbar vessel hemodynamics, and the reproducibility has already been shown [31]. In this study, we evaluate the hemodynamic changes in retrobulbar vessels by CDI to investigate the effect of acupuncture on OAG eyes.

2. Subjects

After the ethics committee approved the study, 11 patients diagnosed with OAG (20 eyes with OAG) were enrolled in this study. The patients received standard medical treatment for at least 3 months. The patients who had an experience of laser trabeculoplasty, any ocular surgery, or inflammation within the past year were excluded in the present study.

Table 1: Characteristic data of the patients with open-angle glaucoma.

Variable	Value
Number of patients	11
Age (years)	63 ± 11
Sexuality (male, female)	(1, 10)
Number of eyes with glaucoma	20
Best corrected visual acuity	1.1 ± 0.3
Spherical equivalent (D)	−1.6 ± 3.2
Humphrey automated perimeter	
Mean deviation (dB)	−11.5 ± 7.8
Pattern standard deviation (dB)	10.2 ± 4.5
OCT RNFL thickness (μm)	70.5 ± 21.8
The number of topical medications	
None	1
One kind	4
Two kinds	1
More than three kinds	5

3. Methods

3.1. Acupuncture. On the trial days, the patients arrived under regular medications. They received acupuncture therapy as follows in the morning. The acupoints were selected on the basis of the principles of traditional Chinese medicine. Acupuncture was performed for 15 min using disposable stainless steel needles (0.16 mm or 0.20 mm × 40 mm; Seirin Co. Ltd., Shizuoka, Japan) at acupoints Cuanzhu (BL2), Taiyang (M-HN9), Sibai (ST2), Zusanli (ST36), Sanyinjiao (SP6), Taixi (KI3), and Taichong (LR3) bilaterally while the patient was in the supine position and at acupoints Fengchi (GB20), Ganshu (BL18), and Shenshu (BL23) bilaterally while the patient was in the prone position for 15 min. Each needle was simply inserted without any intention of eliciting specific responses (e.g., de-qi feelings) to a depth of approximately 20 mm at acupoints ST36, SP6, KI3, GB20, BL18, and BL23. For acupoints BL2, M-HN9, ST2, and LR3, the needles were inserted to a depth of approximately 3–10 mm. Neither needle manipulation techniques nor other auxiliary interventions were used. Five licensed acupuncturists and one physician-acupuncturist with over 5 years of acupuncture experience administered the acupuncture treatment.

3.2. Measurements. To minimize the effects of diurnal variation, all measurements were recorded at the same time of the day (between 10 AM and 11 AM) for each patient by the same examiner. As a control, the subjects received the measurements of the systemic hemodynamics, retrobulbar vessel hemodynamics, and IOP that were performed at rest and one hour after rest. One month later, they received the same measurements before and after acupuncture treatment. The systemic hemodynamics was measured by an oscillometer and the hemodynamics in retrobulbar vessels was measured by ultrasound (LOGIQ e, GE Healthcare, Tokyo, Japan). The ultrasound measurements were performed after 10-minute rest in an air-conditioned room, avoiding any pressure on the eye, with the patients in the supine position. CDI was performed with a 13 MHz linear transducer for retrobulbar vessels such as the ophthalmic artery (OA), central retinal artery (CRA), and short posterior ciliary artery (SPCA). The OA was examined approximately 20 mm behind the globe (Figure 1(a)), the CRA was examined within 5 mm of the retrolaminar portion of the optic nerve (Figure 1(b)), and the temporal SPCA was examined approximately 5–10 mm behind the globe (Figure 1(c)). All blood flow velocity waveforms were measured at the corrected Doppler angle. Resistive index (RI: (peak systolic velocity − end-diastolic velocity)/peak systolic velocity) was also measured in each retrobulbar vessel.

3.3. Statistical Analysis. Statistical analysis was performed with the SPSS software (version 16.0, SPSS Japan Inc., Tokyo, Japan). The parameters between before and after acupuncture or between control and acupuncture were compared by paired t-test.

4. Results

Table 1 shows the characteristics of the subjects. One male and ten female glaucoma patients with a mean age of 63 ± 11 years were observed. The systemic hemodynamic parameters including heart rate, blood pressure, and IOP are shown in Table 2. The blood pressure and heart rate did not change significantly by acupuncture.

The IOP level significantly decreased by acupuncture compared with before acupuncture ($P < .05$). The Δ value of IOP also significantly decreased by acupuncture compared with control ($P < .01$) (Table 2).

Retrobulbar vessel RI in the OA, CRA, and SPCA is shown in Table 3. The RI in the CRA and SPCA decreased

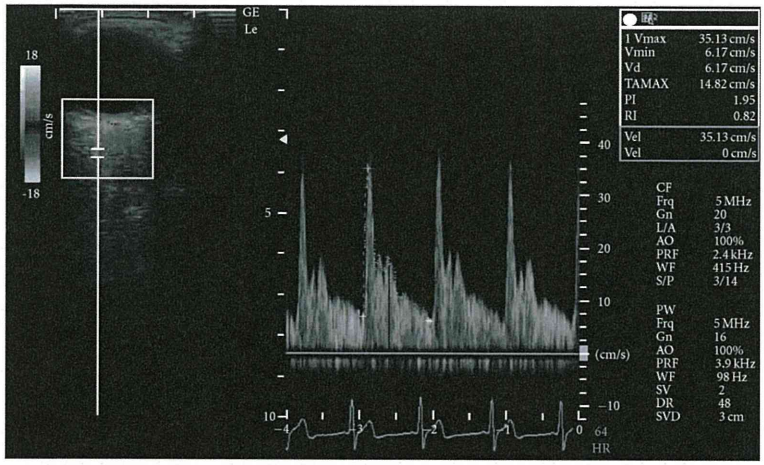

(a)

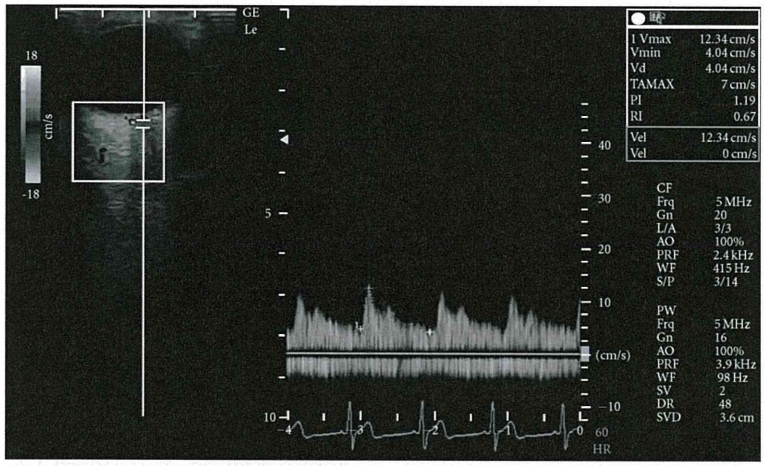

(b)

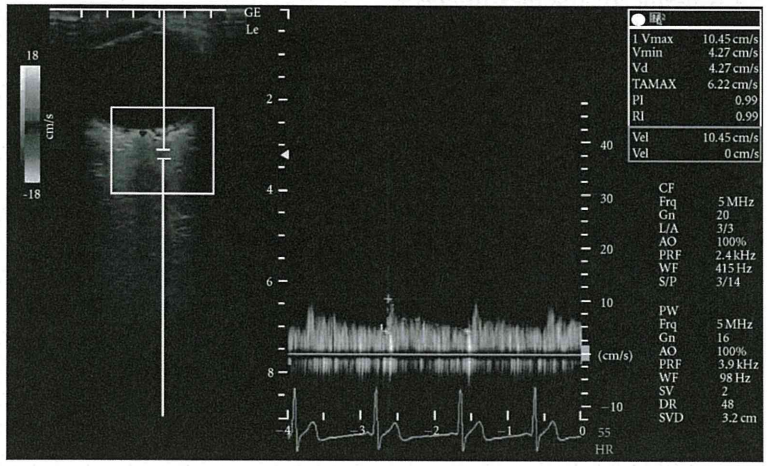

(c)

FIGURE 1: Horizontal scans by color Doppler imaging through the globe showing the (a) ophthalmic artery, (b) central retinal artery, and (c) short posterior ciliary artery.